



High-yield synthesis of BTEX over Na-FeAlO_x/Zn-HZSM-5@SiO₂ by direct CO₂ conversion and identification of surface intermediates

Malayil Gopalan Sibi^{a,b,c}, Muhammad Kashif Khan^{a,b,c}, Deepak Verma^{a,b,c}, Wonjoong Yoon^c, Jaehoon Kim^{a,b,c,*}

^a SKKU Advanced Institute of Nanotechnology (SAINT), Sungkyunkwan University, 2066 Seobu-Ro, Jangan-Gu, Suwon, Gyeong Gi-Do 16419, South Korea

^b School of Mechanical Engineering, Sungkyunkwan University, 2066 Seobu-Ro, Jangan-Gu, Suwon, Gyeong Gi-Do 16419, South Korea

^c School of Chemical Engineering, Sungkyunkwan University, 2066 Seobu-Ro, Jangan-Gu, Suwon, Gyeong Gi-Do 16419, South Korea

ARTICLE INFO

Keywords:

CO₂ conversion
Aromatic synthesis
Modified Fischer–Tropsch synthesis
Operando diffuse reflectance infrared Fourier-transform spectroscopy

ABSTRACT

We present a tandem catalyst consisting of Na-promoted bifunctional FeAlO_x (Na-FeAlO_x) and Zn-doped HZSM-5, the outer surface of which was coated with a SiO₂ layer (Zn-HZSM-5@SiO₂). This tandem catalyst afforded a high BTEX space-time yield of 4.0 mmol g⁻¹ h⁻¹ with a CO₂ conversion of 45.2%. The selectivities toward BTEX were tuned by controlling the nature, density, and distribution of the Brønsted acid sites of the zeolites, in addition to adjusting the proximity between the Fe-based and zeolitic active sites. In situ operando experiments revealed the role of Zn-HZSM-5@SiO₂ not only in dehydroaromatization, but also in CO₂ adsorption, reverse water-gas shift reactions, and C–C coupling reactions. The findings of this study are promising for designing a tandem catalyst to directly convert CO₂ to BTEX in high yields, and also provide novel insights into the reaction intermediates for this tandem catalyst.

1. Introduction

The production of transportation fuels and platform chemicals via the thermocatalytic conversion of CO₂ with green hydrogen is among the most promising strategies for mitigating high anthropogenic CO₂ emissions and addressing challenges associated with the use of renewable energy. This strategy can significantly contribute to the development of a circular economy [1,2]. However, owing to the inherent inertness of CO₂ ($\Delta G_{298\text{ K}}^0 = -394.4\text{ kJ mol}^{-1}$) and the high energy barrier of the C–C coupling reaction [3], the direct conversion of CO₂ into long-chain hydrocarbons and platform chemicals with high yields is considerably challenging. Various types of tandem catalysts have been proposed to synthesize C₅₊ hydrocarbons [4], olefins [5,6], paraffins [7], isoparaffins [8], alcohols [9,10], and aromatics [11–26]. Among these, aromatics such as benzene (B), toluene (T), ethylbenzene (E), and xylene (X), collectively denoted as BTEX, are the most valuable petrochemical products. They are widely used in various fields, such as in the production of commodity plastics, engineering plastics, paints, adhesives, sporting goods, clothing, electronic and display materials, and packaging. The substantial use of aromatics in modern life has

contributed to increasing global carbon emissions. Therefore, the development of a sustainable, carbon-neutral method of producing aromatics (or more desirably, BTEX) is imperative. Currently, aromatics are produced in petroleum industries by the catalytic reforming (a combination of cyclization and dehydrogenation reactions) of heavy naphtha (C₆–C₁₂ hydrocarbons).

Two pathways have been proposed for the direct conversion of CO₂ to aromatics: methanol-mediated and modified Fischer–Tropsch synthesis (FTS). In the former pathway [11,12,16,21–23,25], CO₂ is first converted into methanol, following which methanol is converted to olefins, and finally, the olefins are converted to aromatics. In the latter pathway, CO is first produced from CO₂ via a reverse water–gas–shift (RWGS) reaction. The produced CO is subsequently converted to C₂₊ hydrocarbons using FTS, which are then finally converted to aromatics [13,17–20,26]. Thus, the multiple steps involved in converting CO₂ to aromatics require the design of tandem cascade catalysts. In the methanol-mediated pathway, most tandem catalysts were prepared by combining the catalysts used for converting CO₂ to methanol with microporous MFI-type zeolites (HZSM-5(x), where x indicates the Si/Al ratio). Examples of such catalysts include ZnAlO_x/HZSM-5 [11],

* Correspondence to: School of Mechanical Engineering, School of Chemical Engineering, SKKU Advanced Institute of Nanotechnology (SAINT), Sungkyunkwan University, 2066 Seobu-Ro, Jangan-Gu, Suwon, Gyeong Gi-Do 16419, South Korea

E-mail address: jaehoonkim@skku.edu (J. Kim).

<https://doi.org/10.1016/j.apcatb.2021.120813>

Received 15 July 2021; Received in revised form 10 September 2021; Accepted 8 October 2021

Available online 12 October 2021

0926-3373/© 2021 Elsevier B.V. All rights reserved.

ZnZrO/HZSM-5(100) [12], ZnO/ZrO₂/HZSM-5(300) [25], Cr₂O₃/HZSM-5(80) [23], Cr₂O₃/Zn-doped HZSM-5(80)@SiO₂ [16], ZnCrO_x/HZSM-5(280) [22], and ZnO–ZrO₂ aerogel/H-ZSM-5(68) [21]. According to Table S1, the methanol-mediated pathway produces highly selective aromatics (40–76%, excluding CO); however, the low CO₂ conversion (5–28%) and high CO selectivity (13–47%) should be analyzed carefully. In the modified FTS pathway, traditional Fe-based FT catalysts were composited with HZSM-5 to continue the tandem catalytic reactions. Examples of such catalysts include Na–Fe₃O₄/HZSM-5(320) [26], Na–Fe/HZSM-5(12.5) [24], KO₂–Fe₂O₃/HZSM-5(13) [18], Na–ZnFeO_x/S-HZSM-5(12.5) [13], FeK_{1.5}/HSG=HZSM-5(25) [20], and Na–Fe@C/hollow-structured HZSM-5 [17]. Compared to the methanol-mediated pathway, the modified FTS pathway afforded relatively high CO₂ conversion (30–50%) with moderate aromatic selectivity (25–68%). This moderate aromatic selectivity could be attributed to differences in the optimum reaction conditions for the modified FTS and the conversion of hydrocarbons to aromatics, besides the limitations posed by the Anderson–Schulz–Flory distribution.

Despite the worth of BTEX, only a few studies on converting CO₂ to aromatics using both, the methanol-mediated and modified FTS pathways, have discussed the selectivities, yields (Table S1), and their improvement. Owing to its shape selectivity, which originates from its unique zeolitic topology, pore size, and suitable acidity, HZSM-5 has been widely used in the production of aromatics from light alkanes [27–33]. Metal- or metal oxide-modified HZSM-5 has been demonstrated to be effective in improving the selectivity toward aromatics from various feedstocks [29,31,34–38]. For example, performance relationship, mechanistic understanding, and deactivation kinetics of ethane and ethylene aromatization on highly-dispersed zinc species on HZSM-5 have been discussed [29,39,40]. Identification of reductive zinc species during the aromatization of n-pentane and the role of Lewis acid sites in the Zn-doped HZSM-5 in the conversion of isobutane to aromatics was studied [41,42]. Detailed reaction mechanisms during the dehydrogenation alkane on the Zn species in the Zn-doped HZSM-5 (e.g., Zn²⁺, [Zn–O–Zn]²⁺) were discussed [39]. However, the B, T, and *para*-xylene (PX) produced within the micropores of zeolite tend to undergo alkylation when they diffuse out of the micropores to near the pore mouth and the external surface. This induces their transformations to three-, tetra-, hepta-, and hexa-alkyl-substituted aromatics, which, in turn, results in decreased BTX selectivity. To selectively passivate the acidity at the external surface and pore mouth, coating with an inert material (e.g., SiO₂) has been proposed [11,13,16,19,23,24,28]. However, the role of heterometal doping in HZSM-5 toward controlling the Brønsted acid sites (BASs) of the zeolites as well as maintaining synergy between the Fe sites and zeolites during the direct conversion of CO₂ to aromatics remains to be investigated.

Previously, we had demonstrated that the use of Na-promoted iron aluminum oxide (Na–FeAlO_x) with an Fe/Al weight ratio of 1:1 resulted in high CO₂ conversion and high α -olefin selectivity. These high values were attributed to high CO adsorption, high H₂ adsorption, accelerated FTS, and the suppression of undesirable water–gas–shift (WGS) reactions [6]. These advantages of Na–FeAlO_x make it an excellent candidate for the synthesis of aromatics when incorporated with HZSM-5. In this study, we achieved the highly selective production of BTEX by directly converting CO₂ over a tandem catalyst consisting of Na–FeAlO_x and Zn-doped HZSM-5, the outer surface and pore mouth of which were coated with SiO₂ (Na–FeAlO_x/Zn–HZSM-5@SiO₂). To optimize the BTEX yields, the properties of HZSM-5 were controlled by adjusting the Si/Al ratio of zeolite, Zn-doping level, and SiO₂ coating thickness. Subsequent sections in this paper discuss the effects of various types of catalysts and operating conditions on the CO₂ conversion and product selectivity. By conducting in situ operando time-resolved in situ diffuse reflectance infrared Fourier-transform spectroscopy (DRIFTS) experiments, the differences among the reaction intermediates of the Na–FeAlO_x, Zn–HZSM-5@SiO₂, and Na–FeAlO_x/Zn–HZSM-5@SiO₂

catalysts were analyzed. Extensive analyses allowed us to elucidate the reaction mechanisms and synergistic effect between Na–FeAlO_x and Zn–HZSM-5@SiO₂.

2. Experimental section

The supplementary data provides a detailed description of the experimental procedure. It includes descriptions of the materials used for the synthesis of the catalysts. It also includes information on the methods used for catalyst synthesis, CO₂ conversion, catalyst evaluation, and catalyst characterization, including X-ray diffraction (XRD), high-resolution transmission electron microscopy (HR-TEM), scanning electron microscopy (SEM), scanning transmission electron microscopy–energy-dispersive X-ray spectroscopy (STEM-EDS), nitrogen adsorption–desorption, inductively coupled plasma–optical emission spectrometry (ICP-OES), temperature-programmed desorption (of hydrogen, carbon dioxide, and ammonia (H₂–TPD, CO₂–TPD, and NH₃–TPD)), and pyridine, CO₂, and CO DRIFTS. The product was analyzed using online-refinery gas analysis–gas chromatography (RGA–GC), gas chromatography–time-of-flight mass spectrometry (GC–TOF/MS), gas chromatography–flame ionization detection (GC–FID), and high-performance liquid chromatography (HPLC), the details of which are also provided in the supplementary data.

3. Results and discussion

3.1. Performance in the hydrogenation of CO₂ to aromatics

The Na–FeAlO_x/Zn–HZSM-5@SiO₂ catalyst afforded high CO₂ conversion (45.2%) with a high selectivity for aromatics (38.7%, excluding CO) and BTEX (22.8%, excluding CO) at 370 °C, 3.5 MPa, H₂/CO₂ = 3:1, and a gas hourly space velocity (GHSV) of 4000 mL g^{−1} h^{−1}. As listed in Table S1, the Na–FeAlO_x/Zn–HZSM-5@SiO₂ catalyst provided higher space–time yields (STYs) of aromatics (6.8 mmol g^{−1} h^{−1}), PX (1.03 mmol g^{−1} h^{−1}), and BTEX (4.0 mmol g^{−1} h^{−1}) than those in most previous studies. The reduction in the concentration of strong BASs by Zn-doping and the suppression of external acid sites by coating with SiO₂ improved the STYs of BTEX and PX. The following sections discuss these results in detail.

First, CO₂ conversion was evaluated using the Na–FeAlO_x catalyst without incorporating HZSM-5. At 335 °C, 3.5 MPa, a H₂/CO₂ ratio of 3:1, and GHSV of 4000 mL g^{−1} h^{−1}, a CO₂ conversion of 36.8%, C₂–C₄ selectivity of 30.1% (hereafter excluding CO) with an olefin-to-paraffin (O/P) ratio of 8.5, and C₅₊ selectivity of 57.8% with an O/P ratio of 1.6 (Fig. 1) were obtained. Aromatics were not observed to have formed over the Na–FeAlO_x catalyst. Water-soluble organics were negligibly detected in the aqueous phase. Increased concentrations of olefins could reduce the burden of dehydrogenation, and thus, aid in the synthesis of aromatics on the zeolitic micropores [27,43]. As the temperature increased to 370 °C, the CO₂ conversion increased slightly to 47.9%, the C₂–C₄ selectivity decreased to 23.7%, and the C₅₊ selectivity did not change significantly (57.5%). Over the Na–FeAlO_x/HZSM-5(12.5) catalyst (denoted as FZ) prepared by mortar mixing, the CO₂ conversion at 335 °C slightly decreased from 36.8% to 30.9%, while the selectivity towards CO and CH₄ slightly increased from 7.2% to 11.6% and from 12.1% to 17.6%, respectively, compared to those of Na–FeAlO_x. The number of Fe-based active sites was insufficient to continue FTS using the FZ catalyst, which, in turn, could decrease the CO₂ conversion and increase the CH₄ and CO selectivities. CO₂ conversion over the FZ catalyst resulted in the formation of aromatics with 34.3% selectivity. Therefore, the hydrocarbon intermediates produced over the Na–FeAlO_x catalyst diffused into the micropores of HZSM-5(12.5). This resulted in the production of aromatics by acid-catalyzed reactions, including dehydrogenation, oligomerization, isomerization, and aromatization [30,44–48]. However, the selectivities toward BTEX over the FZ catalyst were negligible (< 1.5%, Fig. 1b). Instead, methyl- and ethyl-substituted

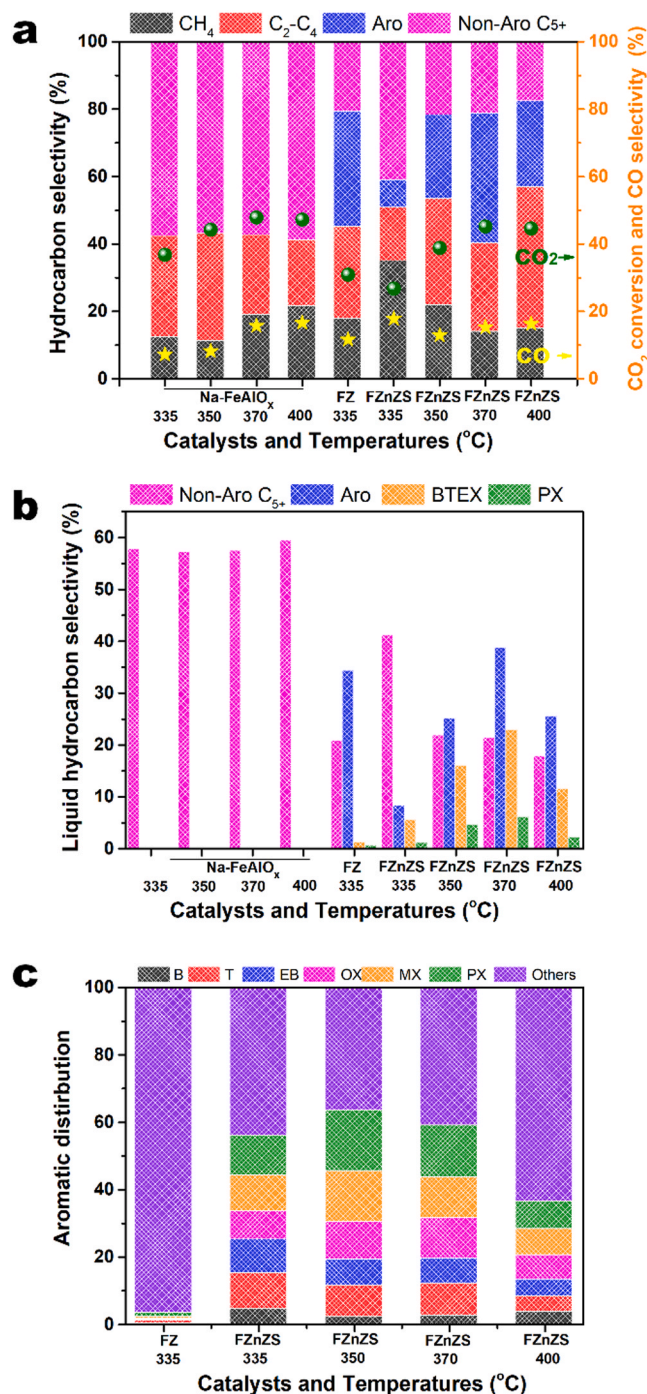


Fig. 1. Hydrogenation of CO₂ over the Na-FeAlO_x, Na-FeAlO_x/HZSM-5(12.5) (FZ), and FeAlO_x/Zn-HZSM-5(12.5)@SiO₂ (FZnZS) catalysts at temperatures from 335° to 400 °C. (a) CO₂ conversion, CO selectivity, hydrocarbon selectivity (excluding CO), (b) liquid hydrocarbon selectivity, and (c) distribution of aromatics. Pretreatment conditions: 450 °C, 3.5 MPa, H₂ flow rate of 50 mL min⁻¹ for 10 h. Reaction conditions: 3.5 MPa, H₂/CO₂ = 1:3, 4000 mL g⁻¹ h⁻¹ (CO₂ = 1000 mL g⁻¹ h⁻¹, H₂ = 3000 mL g⁻¹ h⁻¹). Zn-doping was conducted at 1.0 M concentration and the SiO₂ loading was 45 wt% based on pristine HZSM-5. Non-Aro C₅+, non-aromatic C₅+, Aro, aromatics; B, benzene; T, toluene, EB, ethylbenzene; X, xylene; OX, o-xylene; MX, m-xylene; PX, p-xylene.

benzene, di-ethyl-substituted benzene, tri-methyl-substituted benzene, naphthalene, and methyl-substituted naphthalene were the major aromatics (Fig. S1). This was due to the abundance of BASs on the surface of pristine HZSM-5(12.5) that facilitated the alkylation of B, T, and PX. The high selectivities toward the highly alkyl-substituted aromatics over the FZ catalyst implied that the low Na content in the Na-FeAlO_x catalyst (0.74%) did not significantly neutralize the acid sites present in the micropores and the external surface of pristine HZSM-5(12.5).

As discussed in the introduction section, a well-developed approach to increasing the selectivities of aromatics is to control the acidity of HZSM-5 by heteroatom doping (e.g., with Zn) in the BASs [27–33]. In addition, the undesirable overalkylation and isomerization on the external surface of HZSM-5 can be suppressed by coating a thin SiO₂ layer on the surface and pore mouths of HZSM-5 [11,13,16,19,23,24]. The size of the microchannel of HZSM-5 with 10-membered rings (5.5 Å × 5.1 Å and 5.6 Å × 5.3 Å) was comparable to the kinetic diameters of B, T, and PX (5.85 Å). However, its pore sizes were smaller than the kinetic diameters of *ortho*-xylene (OX, 6.80 Å) and *meta*-xylene (MX, 6.80 Å) and ethyl benzene (EB, 6.00 Å) [49]. Therefore, when the B, T, and PX that had formed inside the micropores diffused out of the pores, a certain amount tended to be converted to OX, MX, and other alkylated aromatics over the acid sites at the pore mouths and the external surface of unmodified HZSM-5 [50]. The minimum kinetic diameter of tetraethoxysilane (TEOS) was larger than the pore mouths of the zeolite. Therefore, only the surface –OH groups on pristine HZSM-5 reacted with TEOS to form Si–O–Si or Si–O–Al bonds, blocking the external acid sites [28,51,52]. To investigate the effects of Zn-doping and the SiO₂ coating on the synthesis of aromatics, CO₂ conversion was conducted over the FeAlO_x/Zn-HZSM-5(12.5)@SiO₂ catalyst (denoted as FZnZS). Zn-doping was conducted using the ion-exchange method in a 1.0 M aqueous Zn(NO₃)₂ solution. At 335 °C, the CO₂ conversion decreased to 26.8%, while the selectivities toward CO and CH₄ drastically increased to 17.8% and 34.8%, respectively. Moreover, the aromatic selectivity decreased to 8.2% compared to that for the FZ catalyst. The lower CO₂ conversion and aromatic selectivity obtained over FZnZS than FZ could be attributed to the diffusion limitation at low temperatures. The hydrocarbon intermediates produced over the active site of Na-FeAlO_x could not be efficiently transported to the micropores of HZSM-5 in the presence of the SiO₂ coating [53]. To overcome this issue, the reaction temperatures were increased. As the temperature was increased from 335° to 370 °C over the FZnZS catalyst, the CO₂ conversion and aromatic selectivity increased significantly from 26.8% to 45.2% and from 8.2% to 38.7%, respectively. However, the selectivities toward CO and CH₄ decreased from 17.8% to 15.3% and from 34.8% to 13.8%, respectively. Thus, the improved transport of hydrocarbon intermediates from the Na-FeAlO_x site to the micropores of Zn-HZSM-5 (12.5)@SiO₂ at high reaction temperatures significantly enhanced the aromatic yields. As the reaction temperature was increased from 335° to 370 °C, the selectivities toward BTEX and PX increased from 5.4% to 22.8% and from 1.0% to 6.0%, respectively (Fig. 1b). Compared to those of the other aromatics, the selectivities of BTEX did not change significantly, and remained within the 56–64% range at 335–370 °C (Fig. 1c). Therefore, control of the acid sites by Zn-doping and SiO₂ coating played an important role in increasing the production of valuable aromatic species. When the temperature was further increased to 400 °C over the Na-FeAlO_x catalyst, there was a slight increase in methanation at the expense of the C₂–C₄ selectivity. Over the FZnZS catalyst at 400 °C, the selectivities toward C₅ and aromatics decreased, while that toward C₂–C₄ increased, compared to those at 370 °C. This could be attributed to the activated secondary hydrocracking reaction at the acid sites of Zn-HZSM-5(12.5).

3.2. Optimization of catalysts and process parameters

To further examine the individual and combined roles of Zn-doping and SiO₂ coating in the conversion of CO₂ and selectivity of aromatics, as

well as to optimize the catalyst compositions, CO₂ conversions for the FZ, Na-FeAlO_x/Zn-HZSM-5(12.5) (denoted as FZnZ), Na-FeAlO_x/HZSM-5(12.5)@SiO₂ (denoted as FZS), and FZnZS catalysts were conducted at temperatures from 335° to 370°C. At the low temperature of 335 °C (Fig. S2a–c), the FZnZ catalyst afforded a slightly higher CO₂ conversion of 43.0% and slightly lower CH₄ selectivity of 14.5% compared to the FZ catalyst (30.9% and 17.6%, respectively). The total aromatic selectivities obtained over the FZ and FZnZ catalysts were similar, while the selectivities toward BTEX over the FZnZ catalyst were significantly higher (9.9%) than those over the FZ (1.1%) catalyst. The Zn-HZSM-5(12.5) catalyst, synthesized by the Zn cation-exchange reaction and subsequent calcination, formed isolated Zn²⁺ ions that were stabilized at the aluminum sites of the zeolite. These were effective in the dehydrogenation of alkanes, which is the initial step in aromatic formation [30,44–47]. Thus, the similar total aromatic selectivities obtained over the FZ and FZnZ catalysts at 335 °C suggested that Zn²⁺ did not contribute to dehydrogenation at low reaction temperatures. A reduction in the external BASs by Zn-doping could effectively suppress the isomerization and alkylation of BTEX over the FZnZ catalyst (Fig. S2c). As shown in Fig. S3, CO₂ hydrogenation over Zn-HZSM-5(12.5) resulted in a much lower CO₂ conversion (6.8%) and higher CH₄ selectivity (91.1%) than Na-FeAlO_x. Thus, a simple physical mixture of Na-FeAlO_x and Zn-HZSM-5(12.5) without any synergistic effects between the two active domains would result in CO₂ conversion and CH₄ selectivity values between those observed for the Na-FeAlO_x and Zn-HZSM-5(12.5) catalysts. Therefore, the higher CO₂ conversion and lower CH₄ selectivity over the FZnZ catalyst compared to those over the Na-FeAlO_x catalyst implied that mortar mixing induced close proximity between the two components. This, in turn, resulted in a synergistic effect on CO₂ conversion, which will be extensively discussed in the operando DRIFTS section. The FZS catalyst afforded significantly higher BTEX selectivities (13.0%) than the FZ catalyst (1.1%). Therefore, blocking the active sites at the surface and pore mouths of HZSM-5(12.5) could effectively suppress the excess alkylation reaction. However, employing Zn-doping as well as SiO₂ coating decreased the CO₂ conversion to 26.8% and aromatic selectivity to 8.2%. Here too, the diffusion limitation in the SiO₂-coated H-ZSM5(12.5) at the low temperature of 335 °C could be responsible for the decreased CO₂ conversion over the FZnZS catalyst.

Increased temperatures had a detrimental effect on the aromatic selectivity over the FZ catalyst (Fig. S2a, d, and g). For example, when the temperature was increased from 335 to 350 and 370 °C, the selectivities toward aromatics produced over the FZ catalyst decreased from 34.3% to 21.5% and 9.9%, respectively. However, the CO₂ conversion increased from 30.9% to 42.3% and 46.8%, respectively. The decrease in the aromatic selectivity at high temperatures could be attributed to the rapid deactivation of pristine HZSM-5(12.5). The enhanced oligomerization of olefins and aromatization at the BASs of pristine HZSM-5(12.5) could accelerate coke formation. The deactivation could also be attributed to dealumination from the zeolite topology, which was generated due to the enhanced formation of water as a byproduct via an improved RWGS reaction at high temperatures. Zn-doping suppressed the deactivation of HZSM-5(12.5) to a certain extent at high temperatures, as observed in the reaction over the FZnZ catalysts at varying temperatures. In contrast to the observations for the FZ and FZnZ catalysts, increasing the reaction temperatures did not significantly change the CO₂ conversion and aromatic selectivity over the FZS catalyst. Over the FZnZS catalyst, a high reaction temperature of 370 °C was beneficial for increasing both, the CO₂ conversion and aromatic selectivity. In addition, the selectivities toward BTEX and PX increased from 5.4% to 22.8% and from 1.0% to 6.0%, respectively, when the temperature was increased from 335° to 370°C over the FZnZS catalyst. Both, Zn-doping and SiO₂ coating, increased the BTEX contents in the total aromatics produced (Fig. S2c, f, and h).

To optimize the process conditions, the CO₂ conversion and the selectivities toward aromatics and BTEX were analyzed at different

pressures, GHSVs, Si/Al ratios of HZSM-5, and Zn-doping levels using the Na-FeAlO_x/Zn-HZSM-5(x)@SiO₂ catalysts. As shown in Fig. S4, when the pressure was increased from 1.5 to 3.5 MPa, the CO₂ conversion slightly decreased from 51.7% to 45.2%. However, the selectivities toward aromatics and BTEX increased significantly from 7.2% to 38.7% and from 3.1% to 22.8%, respectively. Thus, high pressures are beneficial for enhancing the BTEX selectivities.

As shown in Fig. S5, a decrease in the GHSV from 4000 to 2000 mL g⁻¹ h⁻¹ did not significantly affect the CO₂ conversion and product selectivity. An increase in the GHSV from 4000 to 6000 mL g⁻¹ h⁻¹ resulted in a decrease in the selectivities toward aromatics and BTEX, from 38.7% to 4.9% and from 22.8% to 4.1%, respectively. However, the CO₂ conversion increased slightly from 45.2% to 50.9%. At high space velocities, the reaction intermediates that form at the active sites of Na-FeAlO_x may lack sufficient time to diffuse into the micropores of the zeolite.

As the Si/Al ratio in HZSM-5(x) was increased from 23 to 200 in the Na-FeAlO_x/Zn-HZSM-5(x)@SiO₂ catalysts (Fig. S6), the selectivities toward aromatics and BTEX decreased from 38.7% to 16.1% and from 22.8% to 13.8%, respectively. However, the CO₂ conversion (41–45%) and overall C₅₊ selectivity (58–65%) did not change significantly. Considering the important role played by the BASs of HZSM-5 in dehydroaromatization [27,44–48], a decrease in these BASs in the zeolite would affect the formation of aromatics.

To examine the possibility of enhancing the selectivities toward aromatics, BTEX, and PX, the acidity in the micropores of HZSM-5(12.5) was modified by varying the Zn-doping level. As discussed in the previous section, Zn-doping in a 1.0 M Zn(NO₃)₂ solution effectively increased the selectivities toward total aromatics, BTEX, and PX during high-temperature CO₂ conversion. However, excess Zn-doping had a detrimental effect on the aromatic selectivity. As the Zn(NO₃)₂ solution concentration was increased from 1.0 to 1.5 M, the selectivities of total aromatics and BTEX decreased significantly from 38.7% to 16.2% and from 22.8% to 15.8%, respectively. However, the selectivities toward C₂–C₄ and non-aromatic C₅₊ increased from 26.2% to 39.8% and from 21.3% to 28.7% (Fig. S7a and b), respectively. The reduced ability of excess-Zn-doped HZSM-5(12.5) to synthesize aromatics was presumably due to the excess formation of less-active ZnO nanocrystallites for aromatization. Although high Zn-doping levels of 1.5–2.0 M decreased the overall aromatic selectivity, > 90% of the aromatics consisted of BTEX (Fig. S7c).

Blocking external acid sites and the pore mouths of HZSM-5(12.5) with the SiO₂ coating was effective in suppressing the alkylation of aromatics. However, it is important to overcome the hindrance to the transportation of hydrocarbon intermediates to the micropores of HZSM-5. As shown in Fig. S8, increasing the number of SiO₂ coatings on the Zn-doped HZSM-5(12.5) decreased the selectivities toward total aromatics and BTEX, while increasing the selectivity toward non-aromatic C₅₊. A thick SiO₂ coating could hinder the diffusion of reaction intermediates into the micropores. Increasing the number of SiO₂ coatings effectively increased the BTEX content in the total aromatics (Fig. S8c), which confirmed the suppression of overalkylation at the external surface and pore mouths.

Control of the proximity between the metal oxide active site and HZSM-5 played a critical role in establishing the desired synergy for the synthesis of aromatics directly from CO₂ conversion [12,13,17,20,21,23,26]. The proximity between the metal oxide and zeolites was controlled using various mixing methods, including dual-bed, granule mixing, powder mixing, and mortar mixing, in close order. In the methanol-mediated pathway, the closest proximity between the metal oxide active sites and zeolite afforded the highest aromatic selectivity. This could be attributed to the facile transport of the reaction intermediates (e.g., methanol, DME) from the surface of the metal oxide to the micropores of HZSM-5 [12,21,23]. In contrast, in the modified FTS pathway, the closest proximity resulted in detrimental effects on the aromatic selectivity [13,20,26]. One reason for the low aromatic

selectivity in the Fe-based active site/HZSM-5 catalyst was the mutual poisoning of the acid sites in the zeolite and the basic sites of the alkali promoters (e.g., Na and K) [13]. In contrast to previous studies on converting CO₂ to aromatics via the modified FTS pathway, the mortar-mixed Na-FeAlO_x/Zn-HZSM-5(12.5)@SiO₂ catalyst provided a CO₂ conversion and aromatic selectivity that were significantly superior to those obtained from the dual bed and extrudates (Fig. 2). The low content of Na promoters (0.74 wt%, based on the weight of FeAlO_x) and the surface passivation by the SiO₂ coating could suppress the

undesirable migration of Na ions to the micropores of HZSM-5.

3.3. Characterization of active sites

The XRD patterns of the fresh and spent catalysts are shown in Fig. S9a. Following the co-precipitation of Fe(NO₃)₃ and Al(NO₃)₃, the obtained powder was calcined at 600 °C under air flow. The calcined Na-FeAlO_x catalyst exhibited a hematite phase (α-Fe₂O₃) with the (102), (104), (110), and (113) planes at 2θ = 24.1°, 33.3°, 35.7°, and 41.0°, respectively. Peaks associated with the crystalline Al₂O₃ phase were not observed for the calcined Na-FeAlO_x catalyst, indicating the amorphous nature of aluminum oxide in the catalyst [6]. During H₂ reduction at 450 °C, the α-Fe₂O₃ phase was converted to Fe₃O₄ and spinel-structured FeAl₂O₄. The FZnZS catalyst exhibited XRD patterns similar to those of Zn-HZSM-5(12.5)@SiO₂ for 2θ values in the 20–25° range, indicating that mortar mixing did not change the crystalline structure of the zeolite. The XRD pattern of the spent FZnZS catalyst, obtained after 220 h on stream, exhibited the (202), (021), and (510) planes associated with the γ-Fe₅C₂ phase. This phase is a well-recognized active site for FTS in iron-based catalysts [54].

The textural properties of the catalysts, evaluated by collecting N₂ adsorption-desorption isotherms, are presented in Fig. S9b–c and Table S2. Pristine HZSM-5(12.5) exhibited a type I isotherm with a small hysteresis loop, indicating the presence of micropores and mesopores in its structure. The Brunauer–Emmett–Teller (BET) surface area of HZSM-5(12.5) was 402.2 m² g^{−1} and its micropore volume was 0.180 cm³ g^{−1}. The BET surface area of Zn-HZSM-5(12.5) was lower, at 318.8 m² g^{−1}, the reduction in its micropore volume to 0.141 cm³ g^{−1} was due to the formation of ZnO nanocrystallites inside the pores during the ion-exchange reaction. As the SiO₂ layer contributed to the specific surface area, the BET surface area and micropore volume of Zn-HZSM-5(12.5)@SiO₂ were higher (367.9 m² g^{−1} and 0.206 cm³ g^{−1}) than those of Zn-HZSM-5(12.5), indicating the microporous nature of the SiO₂ layer. The reduced Na-FeAlO_x catalyst exhibited a type IV isotherm with a hysteresis loop, indicating a mesoporous structure. The BET surface area of FZnSZ was 220.7 m² g^{−1}, which was higher than that of Na-FeAlO_x, but lower than that of Zn-HZSM-5(12.5)@SiO₂.

The morphologies of Na-FeAlO_x and the zeolites were observed using FE-SEM and HR-TEM. The reduced Na-FeAlO_x catalyst consisted of randomly oriented, nanocrystalline, 20–30 nm-sized Fe₃O₄ particles, which aggregated loosely to form a sponge-like structure (Fig. S10a and b). The interplanar spacings of 2.97, 2.53, and 2.20 Å corresponded to the (220), (111), and (440) planes of Fe₃O₄, respectively (Fig. S10c and d). Zn-doping did not change the elongated prismatic morphology associated with HZSM-5(12.5) (Fig. S10e). ZnO nanocrystallites with sizes of 2–5 nm were embedded in the zeolitic structure (Fig. S10f). The fast Fourier transform (FFT) pattern of Zn-HZSM5(12.5) showed a weak ZnO phase with (101), (002), and (100) planes. The SiO₂ coating did not change the overall morphology of Zn-HZSM5(12.5) (Fig. S10i and j). In Zn-HZSM-5(12.5)@SiO₂, a thin (2–3 nm) amorphous layer coating was observed outside the zeolite particles (Fig. S9k).

The morphologies of the reduced and spent FZnZS catalysts are shown in Fig. 3. In the freshly H₂-reduced FZnZS catalyst, 20–30 nm-sized Na-FeAlO_x particles were deposited on the surface of Zn-HZSM-5(12.5)@SiO₂ (Fig. 3a and b). The uniform distribution of Na-FeAlO_x on Zn-HZSM-5(12.5)@SiO₂ can be observed in the EDS mapping images (Fig. S11). The FFT pattern of the FZnZS catalyst indicates the presence of an Fe₃O₄ phase (Fig. 3c). In the spent FZnZS catalyst, 40–60 nm-sized, irregular-shaped particles were observed (Fig. 3), indicating that the nanosized Na-FeAlO_x particles present in the reduced catalyst were agglomerated during CO₂ hydrogenation. Closer inspection of the agglomerated particles revealed that a dense agglomerate in the center was covered with a thin (approximately 5 nm), amorphous layer, forming a core-shell structure. The FFT image of the core of the particle confirmed the presence of Fe₅C₂ and Fe₃O₄ phases. The agglomerated particle was further examined using high-angle angular dark

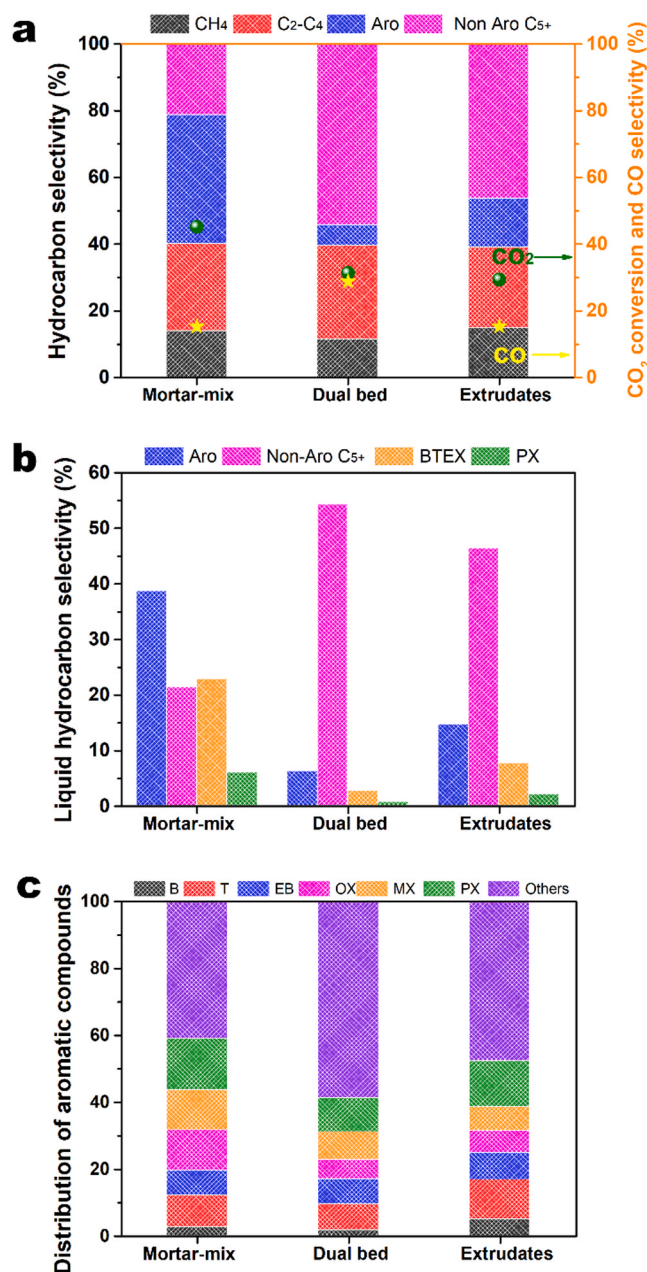


Fig. 2. Hydrogenation of CO₂ over the Na-FeAlO_x/Zn-HZSM-5(12.5)@SiO₂ (FZnZS) catalysts for various modes of mixing. (a) CO₂ conversion, CO selectivity, hydrocarbon selectivity (excluding CO), (b) liquid hydrocarbon selectivity, and (c) distribution of aromatics. Pretreatment conditions: 450 °C, 3.5 MPa, H₂ flow rate of 50 mL min^{−1} for 10 h. Reaction conditions: 3.5 MPa, H₂/CO₂ = 1:3, 4000 mL g^{−1} h^{−1} (CO₂ = 1000 mL g^{−1} h^{−1}, H₂ = 3000 mL g^{−1} h^{−1}). Zn-doping was conducted at 1.0 M concentration and the SiO₂ loading was 45 wt% based on pristine HZSM-5. Non-Aro C₅+, non-aromatic C₅+, Aro, aromatics; B, benzene; T, toluene; EB, ethylbenzene; X, xylene; OX, o-xylene; MX, m-xylene; PX, p-xylene.

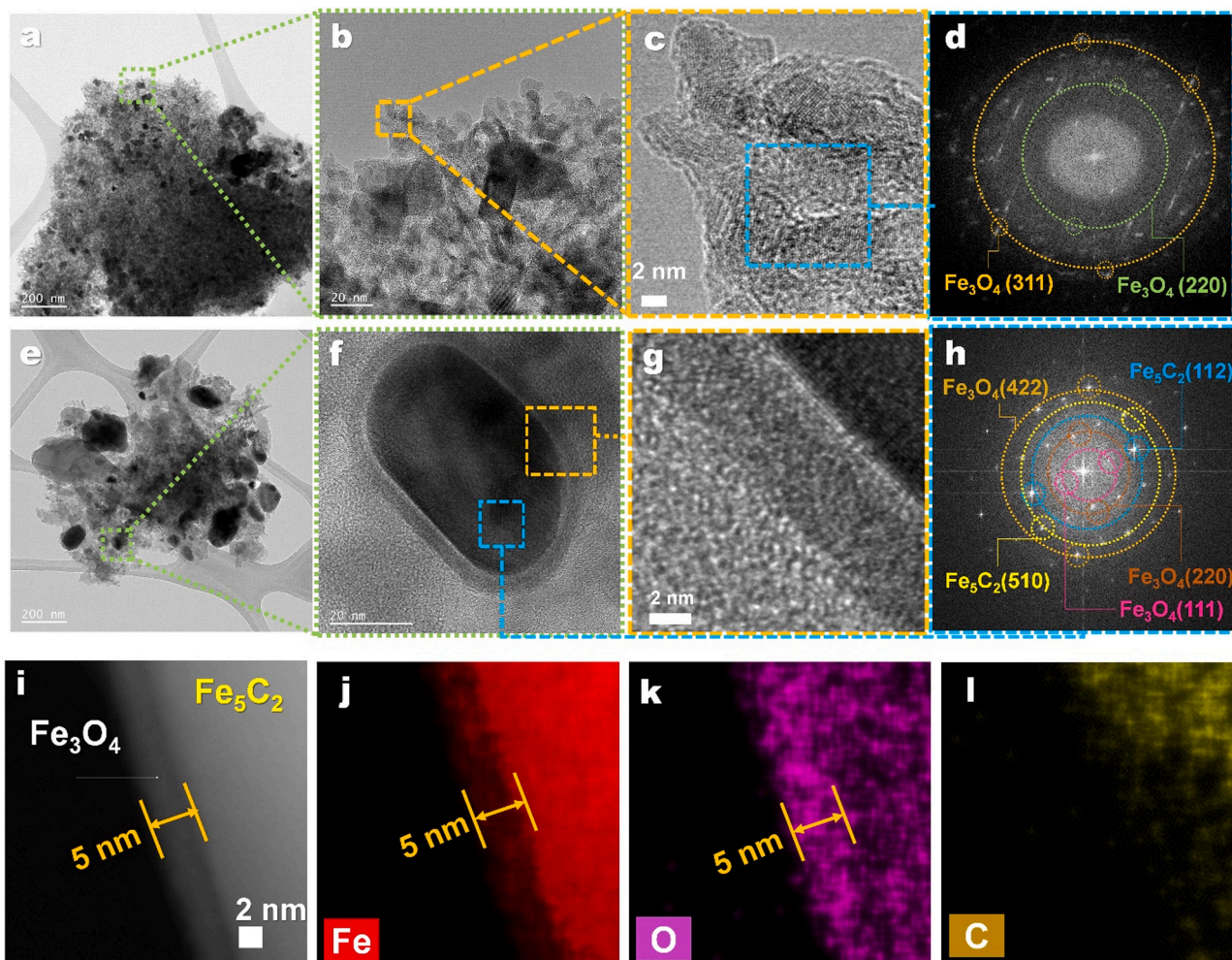


Fig. 3. HR-TEM images and FFT patterns of the (a–d) reduced and (e–h) spent Na-FeAlO_x/Zn-HZSM-5(12.5)/SiO₂ (FZnZS) catalysts. (i–l) STEM-HAADF images and the corresponding EDS images of the spent FZnZS.

field-scanning transmission electron microscopy (HAADF-STEM) images (Fig. 3i–l). The shell consisted of Fe-lean and O-rich phases, while the core consisted of Fe-rich and O-lean phases. Carbon was negligibly detected in the shell; therefore, it can be concluded that the shell mostly comprised an Fe₃O₄ phase, which is the active site for the RWGS reaction. However, the core primarily comprised an Fe₅C₂ phase, which is the active site for the FT reaction [26,54–56].

The surface basicity and CO₂ adsorption behaviors of the zeolitic supports and composite catalysts were investigated using CO₂-TPD profiles (Fig. S12 and Table S3). The basic sites in the catalysts were classified into three categories according to their strengths, i.e., as weak (< 400 °C), medium (400–650 °C), and strong (> 650 °C) desorption sites. On the surface of the Na-FeAlO_x catalyst, CO₂ desorption occurred mainly at the medium sites, with the total amount of CO₂ adsorbed being 0.62 mmol g⁻¹. The medium basic sites of Na-FeAlO_x increased the CO₂/H₂ coverage ratio, rendering them useful for increasing the O/P ratio in the hydrocarbon intermediates [57]. Pristine HZSM-5(12.5) exhibited negligible CO₂ adsorption, while Zn-HZSM-5(12.5) exhibited weak and medium basic sites with a total of 0.114 mmol g⁻¹ of adsorbed CO₂. After coating Zn-HZSM-5(12.5) with SiO₂, the number of weak basic sites increased from 0.093 to 0.166 mmol g⁻¹. This could be caused by the formation of an Si–O⁻ group through the abstraction of a proton from one of the silanol groups during calcination [58,59]. The FZnZS catalyst exhibited much higher CO₂-adsorption strengths in a wide range of desorption regions compared to Na-FeAlO_x and Zn-HZSM-5(12.5)/SiO₂. The CO₂ uptake of the FZnZS catalyst

significantly increased to 1.510 mmol g⁻¹, which was over twice that of Na-FeAlO_x and seven times higher than that of Zn-HZSM-5(12.5)/SiO₂. The CO₂ adsorption exhibited by the powder-mixed FZnZS catalyst was lower than that exhibited by the mortar-mixed FZnZS catalyst. Thus, the close proximity created new interfacial sites between Na-FeAlO_x and Zn-HZSM-5(12.5)/SiO₂ domains that could enhance CO₂ adsorption. As listed in Table S2, the total volume of the FZnZS catalyst is larger than those of Na-FeAlO_x and Zn-HZSM-5(12.5)/SiO₂, which implies additional sites for the CO₂ adsorption.

To examine the total acid sites of the catalysts, NH₃-TPD experiments were performed, the results of which are shown in Fig. S13 and Table S4. The NH₃-TPD profiles of the catalysts presented three desorption regions, termed weak (< 200 °C), medium (200–450 °C), and strong (> 450 °C) acid sites. Owing to the presence of an amorphous AlO_x phase, the Na-FeAlO_x catalyst exhibited strong acid sites (2.35 mmol g⁻¹) that could actively promote the C–C coupling reaction [6]. The NH₃-TPD profile of HZSM-5(12.5) exhibited small peaks at the weak acid site that could be attributed to a cation-bonded silanol group (weak Lewis acid sites, LAs) and a terminal silanol group (weak BAS). The large peaks at the medium acid site could be attributed to the acidic protons at the bridging Si–(OH)–Al sites (strong BAS). The minor and broad peak at the strong acid site could be attributed to the extra Al framework of the Si–(O)–Al sites (strong LAS) and strong BAS [60,61]. Zn-HZSM-5(12.5) exhibited significantly more weak acid sites and lesser medium and strong acid sites than pristine HZSM-5(12.5). This was due to the ion exchange of the Brønsted acid protons in the Si–

(OH)—Al groups with Zn^{2+} ions, which acted as weak LASs [30,62]. After coating Zn-HZSM5-(12.5) with SiO_2 , the strong acid sites increased compared to those of Zn-HZSM5-(12.5), which was possibly due to the formation of an electron-deficient siloxane bridge that acted as an LAS [63]. As expected, the FZnZS catalysts exhibited lower acid site than the Na-FeAlO_x catalyst and higher acid sites than the Zn-HZSM5-(12.5)@SiO₂ support. The weak and medium acid sites of FZnZS were derived from the Zn-HZSM5-(12.5)@SiO₂ support, while its strong acid sites originated from the Na-FeAlO_x catalyst. Thus, in contrast to the CO₂-TPD results, the close proximity between Na-FeAlO_x and Zn-HZSM5-(12.5)@SiO₂ did not create new interfacial sites for NH₃ adsorption. As the Zn-doping level increased from 1.0 to 1.5 M, the total acidity of the FZnZS catalyst decreased significantly from 1.389 to 0.809 mmol g⁻¹. However, a further increase in the Zn-doping level to 2.0 M did not significantly change the total acidity of FZnZS.

The reducing characteristics of the catalysts were analyzed by H₂-TPR and the results are presented in Fig. S14 and Table S5. The broad and small peaks at 350–500 °C in the H₂-TPR profile of Zn(1.0)-HZSM-5(12.5) were attributed to the reduction of ZnO crystallites to Zn⁰. The fraction of ZnO nanocrystallites present in the Zn-HZSM-5(12.5) catalyst, calculated using the amount of H₂ uptake during reduction (0.012 mmol g⁻¹), was 5.1% of the total Zn loading. Thus, approximately 95% of the Zn species in the Zn(1.0)-HZSM-5 framework consisted of non-reducible Zn^{2+} cations, which acted as weak LASs. High reduction temperatures exceeding 600 °C in the Zn(1.5)-HZSM-5(12.5) and Zn(2.0)-HZSM-5(12.5) samples indicated the existence of large ZnO crystals that had formed at high Zn(NO₃)₂ concentrations. The amounts of reducible ZnO in the Zn(1.5)-HZSM-5(12.5) and Zn(2.0)-HZSM-5(12.5) samples increased to 15.4 and 12.5 wt%, respectively. The Na-FeAlO_x catalyst exhibited reduction temperatures of 350–500 and 784 °C, which could be attributed to the conversion of Fe₂O₃ to Fe₃O₄ and Fe₃O₄ to Fe, respectively. The presence of spinel-structured FeAl₂O₄ mitigated the reduction of iron oxides [64]. The FZnZS catalyst exhibited a reduction behavior similar to that of pristine Na-FeAlO_x.

The H₂-TPD data for the catalysts are shown in Fig. S15 and Table S6. The Na-FeAlO_x catalyst underwent high-temperature H₂ desorption above 400 °C. Thus, the presence of an amorphous AlO_x phase facilitated H₂ spillover or subsurface hydrogen adsorption [6]. The FZnZS catalyst underwent significant H₂ desorption at 250–500 °C. Thus, H₂ desorption occurred at moderate temperatures, where CO₂ hydrogenation occurred. The total amount of H₂ desorbed on the FZnZS catalyst was reduced from 0.650 (Na-FeAlO_x) to 0.238 mmol g⁻¹ due to the contribution of Zn-HZSM-5(12.5)@SiO₂ with low H₂-desorbed sites.

To determine the acidic properties of the catalysts, DRIFTS profiles of pyridine and 2,6-di-tert-butylpyridine were acquired, and are shown in Fig. 4 and Fig. S16. The HZSM-5(12.5) sample exhibited IR bands at 1455 and 1614 cm⁻¹ that were associated with the LASs, a band at 1540 cm⁻¹ that was ascribed to the BAS, and bands at 1445 and 1600 cm⁻¹ that were assigned to the hydrogen-bonded LASs [65]. The ratios of LAS to BAS (L/B) were calculated by integrating the areas of the adsorption bands at 1455 and 1540 cm⁻¹, and the results are listed in Table S4. The Zn-HZSM-5(12.5) and Zn-HZSM-5(12.5)@SiO₂ samples exhibited significantly reduced intensities in the BAS at 1540 cm⁻¹, indicating the incorporation of Zn ions into the BASs of HZSM-5. The L/B ratios of Zn-HZSM-5(12.5) and Zn-HZSM-5(12.5)@SiO₂ were higher than pristine HZSM-5(12.5) due to suppression of BASs by the Zn-doping. The dominantly high intensity of the IR band at 1445 cm⁻¹ in the Zn-doped samples indicates that a few Zn species were presented as (ZnOH)⁺, which could act as weak BASs [30,62]. In the Zn-HZSM-5(12.5)@SiO₂ sample, the peak at 1628 cm⁻¹, corresponding to the LAS [66], was prominent. The adsorption spectra of 2,6-di-tert-butylpyridine in Fig. S16 showed that the suppression of BASs at the external surface. The LASs and hydrogen-bonded LASs in the micropores at 1455–1445 cm⁻¹ had significantly reduced, while the LASs on the SiO₂ surface at 1628 cm⁻¹ had increased. This, in turn, indicated the

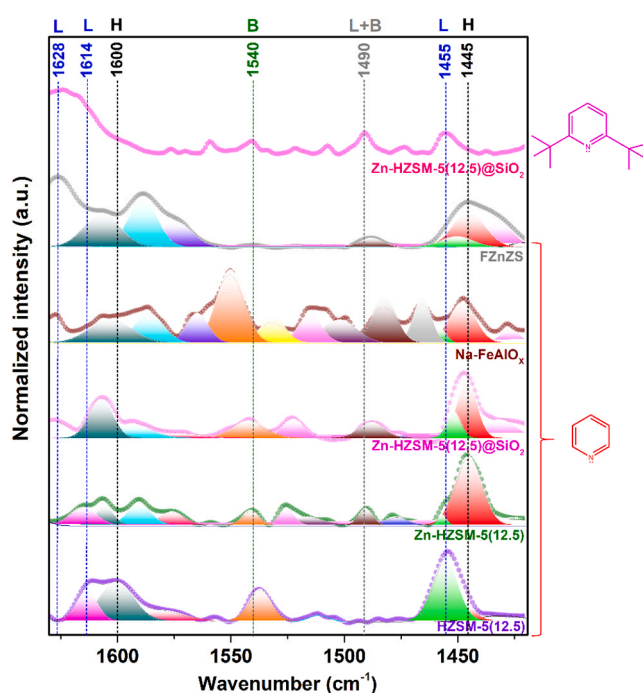


Fig. 4. Pyridine- and 2,6-di-tert-butylpyridine-adsorbed DRIFT spectra of HZSM-5(12.5), Zn-HZSM-5(12.5), Zn-HZSM-5(12.5)@SiO₂, Na-FeAlO_x, and FZnZS.

passivation of external acid sites associated with pristine HZSM-5.

3.4. Identification of reaction intermediates by in situ operando DRIFTS

To understand the reaction mechanism for the formation of aromatics over the FZnZS catalyst, in situ operando DRIFTS experiments were performed to analyze the evolution of the reaction intermediates over the Na-FeAlO_x, HZSM-5(12.5), Zn-doped HZSM-5(12.5)@SiO₂, and FZnZS catalysts. The detailed peak assignments are listed in Tables S7–S9. First, DRIFTS profiles were acquired during the CO₂ pressurization of the DRIFT cell containing a pre-H₂-reduced Na-FeAlO_x catalyst (Fig. 5a). As the CO₂ pressure was increased from 0.1 to 3.0 MPa at 50 °C, the evolution of the IR bands associated with –OH band at 3626 and 3600 cm⁻¹ in the combination band region [67], gaseous CH₄ at 3017 and 1305 cm⁻¹ [68], linearly bonded CO (l-CO) on Fe²⁺ at 2078 cm⁻¹, bridge-bonded CO (b-CO) on Fe⁰ at 1933 and 1916 cm⁻¹ [69–71], and water at 1637 cm⁻¹ [72] was observed. In addition, CO₂-adsorbed species were present in the 2000–1000 cm⁻¹ region. The IR bands at 1457 and 1397 cm⁻¹ could be assigned to the asymmetric and symmetric vibrations ($\nu_{as}(\text{O}—\text{C}—\text{O})$ and $\nu_s(\text{O}—\text{C}—\text{O})$, respectively) of monodentate carbonate (m-CO₃²⁻); those at 1654 and 1287 cm⁻¹ could be assigned to the $\nu_{as}(\text{O}—\text{C}—\text{O})$ and $\nu_s(\text{O}—\text{C}—\text{O})$ of bidentate carbonate (b-CO₃²⁻); those at 1718 and 1473 cm⁻¹ could be assigned to the $\nu_{as}(\text{O}—\text{C}—\text{O})$ and $\nu_s(\text{O}—\text{C}—\text{O})$ of bicarbonate (HCO₃⁻); and those at 1558 and 1362 cm⁻¹ could be assigned to the $\nu_{as}(\text{O}—\text{C}—\text{O})$ and $\nu_s(\text{O}—\text{C}—\text{O})$ of formate (HCOO⁻) [73–75]. The CO₂-adsorbed species became prominent as the pressure was increased to 3.0 MPa. In addition, the peak at 1342 cm⁻¹ could be assigned to methane C–H bending ($\delta(\text{C}—\text{H})_{\text{methylene}}$) [76]. The presence of –OH band could be attributed to the O–H vibration of HCO₃⁻ and the adsorbed water formed during the RWGS reaction [77]. Thus, even at the low temperature of 50 °C, RWGS and hydrogenation reactions between pre-adsorbed H₂ and the adsorbed CO₂ species were activated with increasing pressure. This implies that high pressures are beneficial for continuing the hydrogenation of CO₂.

The DRIFTS profiles obtained from the surface of pristine HZSM-5

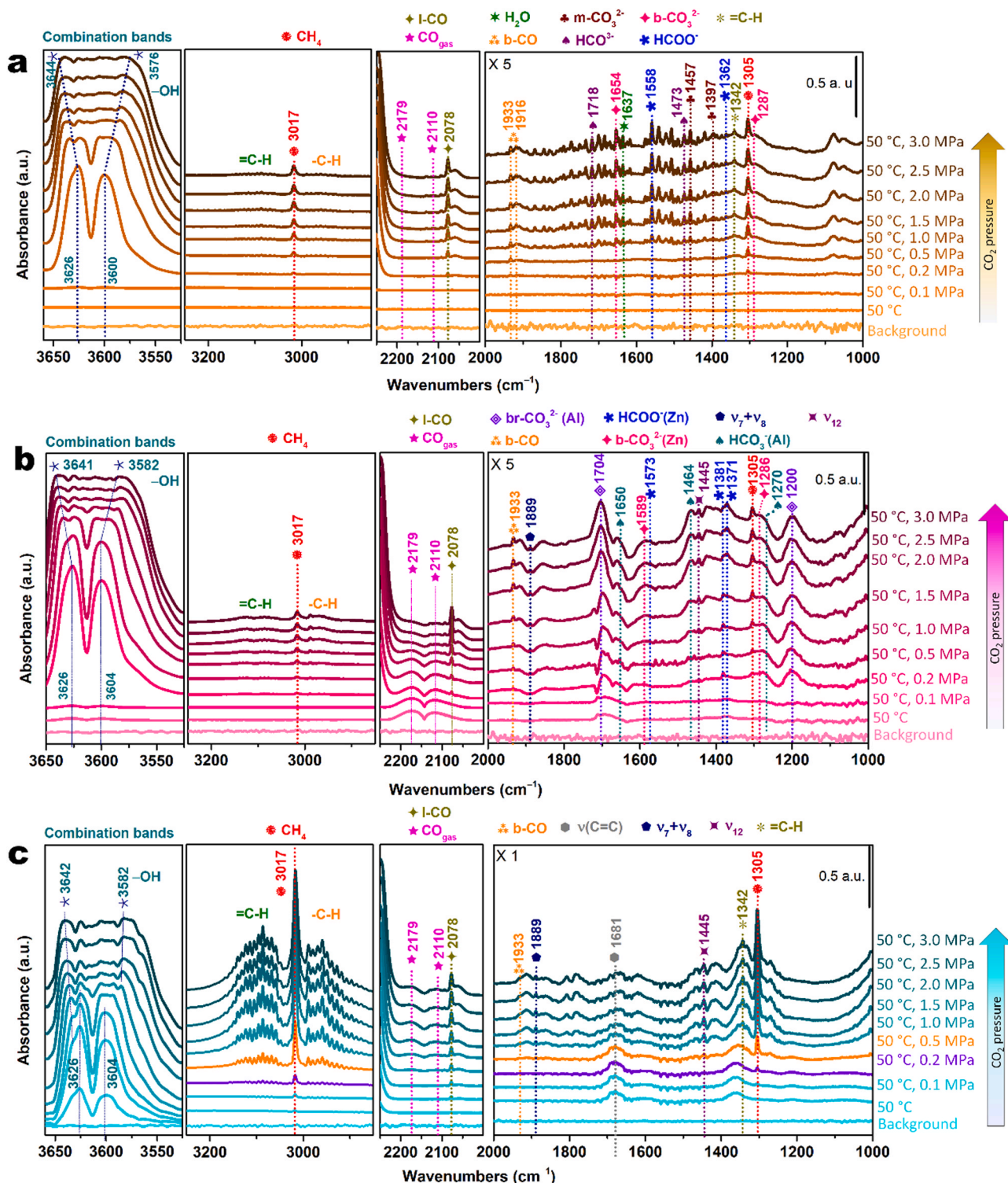


Fig. 5. In situ DRIFTS profiles of CO₂ adsorption with increasing pressure over the (a) Na-FeAlO_x (b) Zn-HZSM-5(12.5)@SiO₂, and (c) FZnZS catalysts. Prior to CO₂ adsorption, the catalysts were reduced at 450 °C for 10 h under a H₂ flow of 50 mL min⁻¹ in the DRIFT cell. Subsequently, the DRIFT cell was evacuated and purged with a N₂ flow of 30 mL min⁻¹ for 2 h to remove H₂. It was then naturally cooled to 50 °C. The DRIFT cell was then pressurized with CO₂ at 3.0 MPa and the spectra were collected as the pressure was increased from 0.1 to 3.0 MPa at 50 °C under a CO₂ flow of 50 mL min⁻¹.

(12.5) when the CO₂ pressure was increased from 0.1 to 3.0 MPa at 50 °C exhibited peaks associated with the CO₂-adsorbed species (b-CO₃²⁻ [78], HCO₃⁻ [75,79], and -OH), I-CO, water, and CH₄ (Fig. S17a and Table S8). In addition, peaks associated with ethylene vibrations (ν_9 at 3125 cm⁻¹, $\nu_2 + \nu_{12}$ at 3079 cm⁻¹, ν_{11} at 2989 cm⁻¹, $\nu_6 + \nu_{10}$ at 2048 cm⁻¹, $\nu_7 + \nu_8$ at 1889 cm⁻¹, and ν_{12} at 1445 cm⁻¹) [80] were

observed. The ethylene adsorption peaks on pristine HZSM-5(12.5) with CO₂ adsorption were verified by matching with those on FZnZS (Fig. S17b). Thus, the presence of the CO₂-adsorbed species, CO, and ethylene on HZSM-5(12.5) indicates that a certain degree of RWGS and C-C coupling reactions occurred due to the presence of surface -OH groups on pristine H-ZSM5(12.5) [75,79,81,82]. A plausible reaction

mechanism for the formation of ethylene species on the pristine H-ZSM5 (12.5) and Zn-doped HZSM-5(12.5) is given in Fig. S18.

The DRIFTS profiles from the surface of Zn-HZSM-5(12.5)/SiO₂ differed significantly from those obtained from pristine HZSM-5(12.5) (Fig. 5b, Table S9). On the surface of Zn-HZSM-5(12.5)/SiO₂, the formation of CH₄ and ethylene was highly suppressed, while the formation of CO₂-adsorbed species (b-CO₃²⁻(Zn) [83,84], HCO₃⁻(Al) [75,79], and HCOO⁻(Zn) [85,86]) was initiated. In addition, bridged CO₃²⁻ species (br-CO₃²⁻) at 1704 and 1200 cm⁻¹ [79] and gaseous CO at 2179 and 2110 cm⁻¹, which were not observed in the DRIFTS profiles of the Na-FeAlO_x and HZSM-5(12.5) catalysts, were detected on the surface of Zn-HZSM-5(12.5)/SiO₂. The polarization of the CO₂ molecule caused by the strong electrostatic field of bivalent Zn²⁺ in the micropores could be responsible for the formation of br-CO₃²⁻ [87]. The formation of gaseous CO over Zn-HZSM-5(12.5)/SiO₂ indicated that the RWGS reaction was activated at the Zn site [88]. Thus, compared to H-ZSM5 (12.5), the hydrogenation of CO₂ to CH₄ and ethylene was suppressed (which could be caused by the inactive SiO₂ coating), while the RWGS of CO₂ to CO was activated at the Zn site. Therefore, the Zn-HZSM-5(12.5)/SiO₂ catalyst played a role not only in aromatization, but also in the CO₂ adsorption, RWGS, and C-C coupling reactions.

The adsorption spectra of CO₂ on the FZnZS catalyst are shown in Fig. 5c. The intensities of IR bands associated with the C-H stretching vibrations of alkene and alkane ($\nu(\text{C-H})$ and $\nu(\text{-C-H})$, respectively) at 3170–3040 and 3000–2850 cm⁻¹, respectively, [89] and CH₄ were significantly increased compare to those of the Na-FeAlO_x and Zn-HZSM-5(12.5)/SiO₂ catalysts under identical operando conditions. In addition, the bands at 1342 and 1681 cm⁻¹, which could be assigned to $\delta(\text{C-H})_{\text{methyne}}$ and alkenyl C=C ($\nu(\text{C=C})_{\text{alkene}}$) [76], respectively, increased with increasing CO₂ pressure. The gaseous CO, l-CO, and ethylene bands were maintained with increasing CO₂ pressure, while the bands associated with the CO₂-adsorbed species were observed in traces on the surface of the FZnZS catalyst. These results indicate that the pre-adsorbed H₂ on the FZnZS catalyst induced the rapid transformation of the CO₂-adsorbed species to CO and hydrocarbons. Therefore, highly activated, concurrent CO₂ conversion occurred on the Na-FeAlO_x and Zn-HZSM-5(12.5)/SiO₂ sites in the composite catalyst, which could contribute to an increase in the overall conversion of CO₂ to olefins.

After the DRIFT cell was pressurized with CO₂ at 3.0 MPa and 50 °C, its temperature was increased to 370 °C while maintaining the same pressure. H₂ flow was subsequently introduced into the cell to observe the CO₂ hydrogenation behaviors over the catalysts. On the surface of Na-FeAlO_x (Fig. 6a), the desorption of CH₄ was observed during temperature ramping, while the intensity of l-CO did not change significantly. In the initial 38 min of H₂ flow, bands associated with gaseous CO began to appear. As the H₂ flow time increased to 120 min, the intensity of the bands associated with the CO₂-adsorbed species, gaseous CO, $\nu(\text{C-H})$, and $\nu(\text{-C-H})$ increased. Thus, under sufficient H₂ flow, the RWGS and FTS were activated over the Na-FeAlO_x catalyst.

On the surface of the Zn-HZSM-5(12.5)/SiO₂ catalyst (Fig. 6b), the bands associated with $\nu(\text{C-H})$, $\nu(\text{-C-H})$, CH₄, $\delta(\text{C-H})_{\text{methyne}}$, and gaseous CO began to appear in the initial 46 min of H₂ flow. With increasing H₂ flow time to 120 min, the intensities of the bands associated with C₂₊ ($\nu(\text{C-H})$, $\nu(\text{-C-H})$, and $\delta(\text{C-H})_{\text{methyne}}$) significantly increased, indicating that the enhanced C-C coupling reaction highly activated the formation of C₂₊ hydrocarbons in the micropores of the zeolite. The decrease in the intensity of the gaseous CO band with increasing H₂ flow time over the Zn-HZSM-5(12.5)/SiO₂ catalyst, which is in contrast with the behavior of Na-FeAlO_x, suggests that the RWGS reaction diminished at the Zn site with sufficient H₂ flow. On the surface of the FZnZS catalyst (Fig. 6c), the intensities of the CO and \geq C₂ hydrocarbon bands began increasing at 52 min of H₂ flow, reached their maximum at 90 min of H₂ flow, and maintained their values at the end of the 120 min-H₂ flow. The intensities of the bands associated with CH₄ and C₂₊ on the FZnZS catalyst were higher than those over the Na-FeAlO_x catalyst, indicating that more active CO₂ methanation and

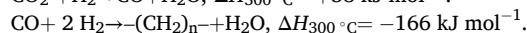
C-C coupling reactions occurred on the FZnZS catalyst. Thus, the CO produced over the Fe and Zn sites was converted to lower olefins at the amorphous AlO_x site and BAS in the zeolite. These lower olefins were subsequently converted to long-chain hydrocarbons and aromatics over the acid sites in the micropores of Zn-doped HZSM-5(12.5).

A mixture of H₂ and CO₂ with a H₂/CO₂ ratio of 3:1 at 370 °C and 3.0 MPa as a feed gas was flowed over the reduced FZnZS catalyst, and in situ operando DRIFTS profiles of the same were acquired (Fig. S19a and b). The changes in the IR band intensities of the major species (CO, CH₄, b-CO₃²⁻, HCOO⁻, aromatics) when the pressure and temperature were increased to 3.0 MPa and 370 °C, respectively, and the flow time was subsequently increased to 260 min, are shown in Fig. 7a. As the pressure and temperature of the DRIFT cell were increased to 3.0 MPa and 100 °C, respectively, the formation of CH₄, C₂₊, and gaseous CO was initiated. With a further increase in the temperature to 330 °C, the intensities of the IR bands associated with m-CO₃²⁻, HCOO⁻, and gaseous CO continued to increase. The intensities remained constant, however, for a further increase in temperature to 370 °C. The band associated with the C=C stretching vibration of the aromatic ring ($\nu(\text{C-H})_{\text{aromatics}}$) at 1510 cm⁻¹ [76] began to appear at 200 °C, and the intensity of the $\nu(\text{C-H})_{\text{aromatics}}$ band increased when the temperature was increased to 370 °C. Thus, high reaction temperatures were favorable for the formation of aromatics, while the activities of RWGS and FT did not change significantly at 330–370 °C. As the flow time was increased to 260 min at 3.0 MPa and 370 °C, the intensity of the $\nu(\text{C-H})_{\text{aromatics}}$ band steadily increased, while that of the CH₄ band gradually decreased; this suggested that the formation of aromatics was facilitated with increasing time.

The temperature/pressure and time evolution behaviors of reaction intermediates on the Na-FeAlO_x catalyst were quite different from those of the FZnZS catalyst, as shown in Fig. 7b and S17c. The RWGS reaction of the Na-FeAlO_x catalyst was slower than that of the FZnZS catalyst. Gaseous CO was initially observed over the Na-FeAlO_x catalyst at 250 °C and 3.0 MPa, and over the FZnZS catalyst at 100 °C and 3.0 MPa. The intensity of the gaseous CO band reached its maximum at 40 min and 370 °C in the time evolution regime over the Na-FeAlO_x catalyst, but at 350 °C and prior to the time evolution regime over the FZnZS catalyst. In addition, the intensities of the bands associated with the CO₂-adsorbed species (m-CO₃²⁻ and HCOO⁻) over the Na-FeAlO_x catalyst were approximately 10 times lower than those over the FZnZS catalyst. The intensity of the CH₄ band over the Na-FeAlO_x catalyst was higher than that over the FZnZS catalyst in the time evolution regime. Therefore, CO₂ adsorption and the RWGS reaction were more activated over the FZnZS catalyst, indicating the synergistic effect between the Na-FeAlO_x and Zn-HZSM-5(12.5)/SiO₂ sites in activating CO₂ hydrogenation.

3.5. Reaction mechanism for the formation of aromatics

Based on the discussion thus far, a plausible reaction mechanism can be proposed for the formation of aromatics over the FZnZS catalyst. CO₂ hydrogenation over Fe-based catalysts proceeds through a two-step process: the initial conversion of CO₂ to CO via RWGS followed by chain propagation.



Although the mechanisms of the RWGS and FTS reactions over the Fe-based catalysts remain unclear due to the complexity of the reaction pathways, the Fe₃O₄ phase has been considered a potential site for the RWGS reaction, and the Fe₅C₂ phase, for the C-C coupling reaction [54, 90]. In the spent FZnZS catalyst, an Fe₅C₂ phase in the core and an Fe₃O₄ layer at the shell were observed (Fig. 3). Such a core-shell structure could efficiently convert CO₂ to CO at the shell; the produced CO is subsequently diffused to the Fe₅C₂ phase in the core to continue the FTS reaction. C₂₊ olefins and C₂₊ paraffins are produced as the major and minor products, respectively. Although the Zn-HZSM-5(12.5)/SiO₂

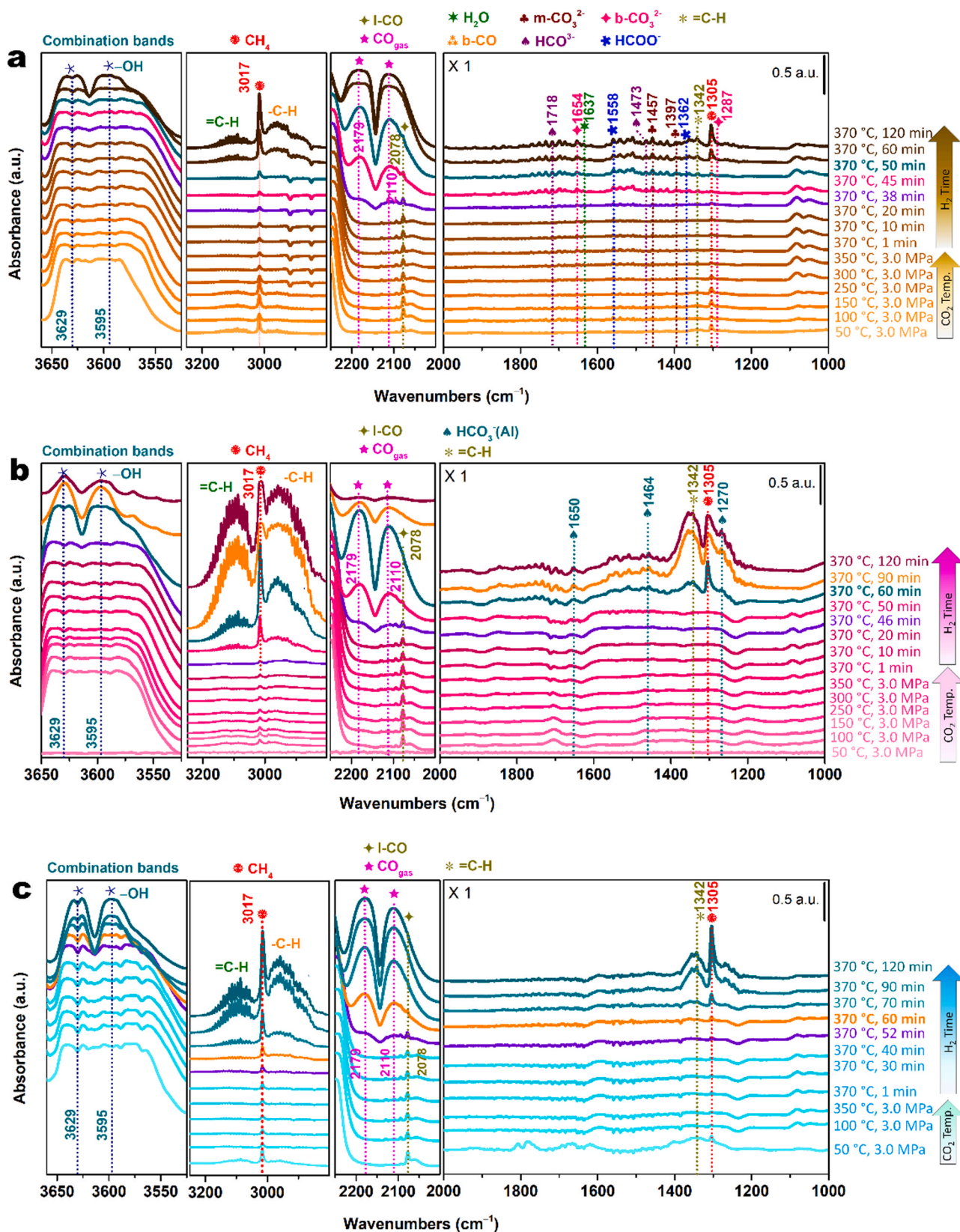


Fig. 6. In situ DRIFTS profiles of CO₂ hydrogenation after the adsorption of CO₂ over the (a) Na-FeAlO_x, (b) Zn-HZSM-5(12.5)/SiO₂, and (c) FZnZS catalysts. Prior to hydrogenation, the catalysts were reduced at 450 °C for 10 h under a H₂ flow of 50 mL min⁻¹. Subsequently, the DRIFT cell was evacuated and purged with a N₂ flow of 30 mL min⁻¹ for 2 h to remove H₂. It was then naturally cooled to 50 °C. The DRIFT cell was then pressurized with CO₂ at 3.0 MPa and 50 mL min⁻¹ as the temperature was increased from 50° to 370 °C. The CO₂ flow at a rate of 50 mL min⁻¹ was maintained at 370 °C for 1 h. The flow gas was then switched from CO₂ to H₂ at a flow rate of 50 mL min⁻¹ at 370 °C and 3.0 MPa.

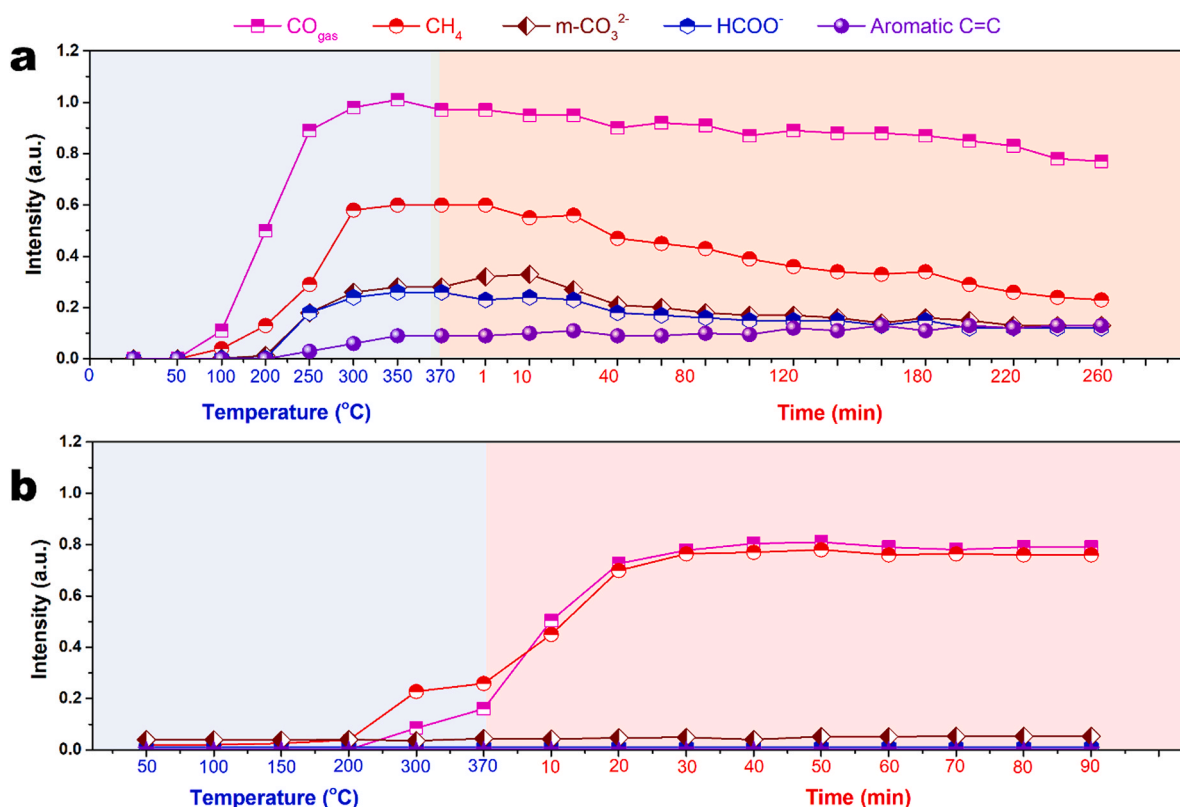


Fig. 7. Evolution of reaction intermediates and products with increasing temperature and time measured using in situ DRIFTS over the (a) FZnZS and (b) Na-FeAlO_x catalysts. See Fig. S18 for the DRIFTS profiles.

support contributes to CO₂ adsorption and the formation of CO and adsorbed hydrocarbons (Figs. 5b and 6b), direct CO₂ hydrogenation over the Zn-HZSM-5(12.5)/SiO₂ support resulted in low CO₂ conversion (5.9%) with high CH₄ selectivity (88.6%) (Fig. S3). However, the FZnZS catalyst exhibited higher activity for the production of C₂₊ hydrocarbons compared to the Na-FeAlO_x catalyst and the Zn-HZSM-5(12.5)/SiO₂ support. This indicates that the CO₂-adsorbed intermediates produced at the active sites in Zn-HZSM-5(12.5)/SiO₂ contribute to C₂₊ hydrocarbon formation at the Fe₃C₂ and zeolitic sites. Thereafter, the C₂₊ hydrocarbons are diffused into the microporous channel of Zn-HZSM-5/SiO₂, where oligomerization into C₆₊ olefins/paraffins occurs at the strong LASs in cooperation with the BASs [91,92]. The produced C₆₊ olefins/paraffins are then transformed into naphthene via hydrogen transfer and cyclization reactions, followed by a series of dehydrogenation steps to produce aromatics [93,94]. The presence of Zn sites in the micropores of HZSM-5(12.5) could accelerate the initial dehydrogenation of alkanes, which could further contribute to the formation of aromatics [29–31,45]. The pore size of the zeolite is approximately equal to the size of the aromatic ring; therefore, the synthesized mononuclear aromatics diffuse out of the pores to the surface and are further alkylated on the BASs at the surface to form alkyl-substituted aromatics.

3.6. Stability of catalyst and its reactive regeneration by coke burning

Fig. 8a shows the long-term stability of the FZnZS catalyst monitored at 370 °C, 3.5 MPa, a H₂/CO₂ ratio of 3:1, and a GHSV of 4000 mL g⁻¹ h⁻¹. The initial CO₂ conversion activity of the FZnZS catalyst was maintained in the 43–50% range for up to 150 h on stream. When the reaction time reached 172 h on stream, a rapid decrease in the CO₂ conversion to 27% was observed. The selectivities toward aromatics and BTEX steadily decreased from 38.7% to 9.1% and from 22.8% to 7.9%, respectively, when the time on stream was increased from 12 to 172 h.

Considering the stable catalytic activity of the Na-FeAlO_x catalyst for up to 450 h on stream [6], significant catalyst deactivation could occur at the zeolitic site. A few aromatics that remained on the surface and in the micropores of the FZnZS catalyst could undergo polymerization to form coke, resulting in a loss of catalytic activity. Thus, after 172 h, the FZnZS catalyst was regenerated by burning coke; the reactor pressure and temperature decreased to 0.1 MPa and 35 °C, respectively, and the reactor system was subsequently flushed with N₂. The reactor temperature was then increased to 250 °C with N₂ purging at 50 mL min⁻¹. Two-step coke burning was conducted until the burned gas flowing downstream was devoid of CO₂, as measured using on-line RGA-GC; the conditions maintained were 5% O₂/Ar at 15 mL min⁻¹ and 450 °C for 6 h and 5% O₂/Ar at 50 mL min⁻¹ and 550 °C for 2 h. The catalyst was then reduced under conditions identical to those maintained while reducing the fresh catalyst, and CO₂ was converted over the regenerated catalyst. The CO₂ conversion and selectivities of the regenerated catalyst toward aromatics and BTEX were similar to those in the initial 24 h of the reaction over the fresh catalyst. By further increasing the reaction time to 320 h on stream, the CO₂ conversion decreased to 30.1% and the selectivities toward aromatics and BTEX decreased to 10.3% and 8.5%, respectively.

There are several reasons for the deactivation of HZSM-5 during the formation of aromatics from olefins and paraffins or directly from CO₂. Some among them include the deactivation of the BASs by water formed as a byproduct, coke formation, and dealumination [17,19,21,24,25, 95–97]. The XRD patterns of the fresh, spent, and regenerated FZnZS catalysts indicate that the crystallinity of the zeolitic structure did not change significantly (Fig. 8b), implying that the removal of aluminum ions from the framework played a minor role in catalyst deactivation. The Fe₃O₄ phase in the spent FZnZS catalyst was completely oxidized to the Fe₂O₃ phase in the regenerated catalyst collected after coke burning. As shown in Fig. S20, the color of the regenerated catalyst changed to brownish red, indicating the presence of the Fe₂O₃ phase. The

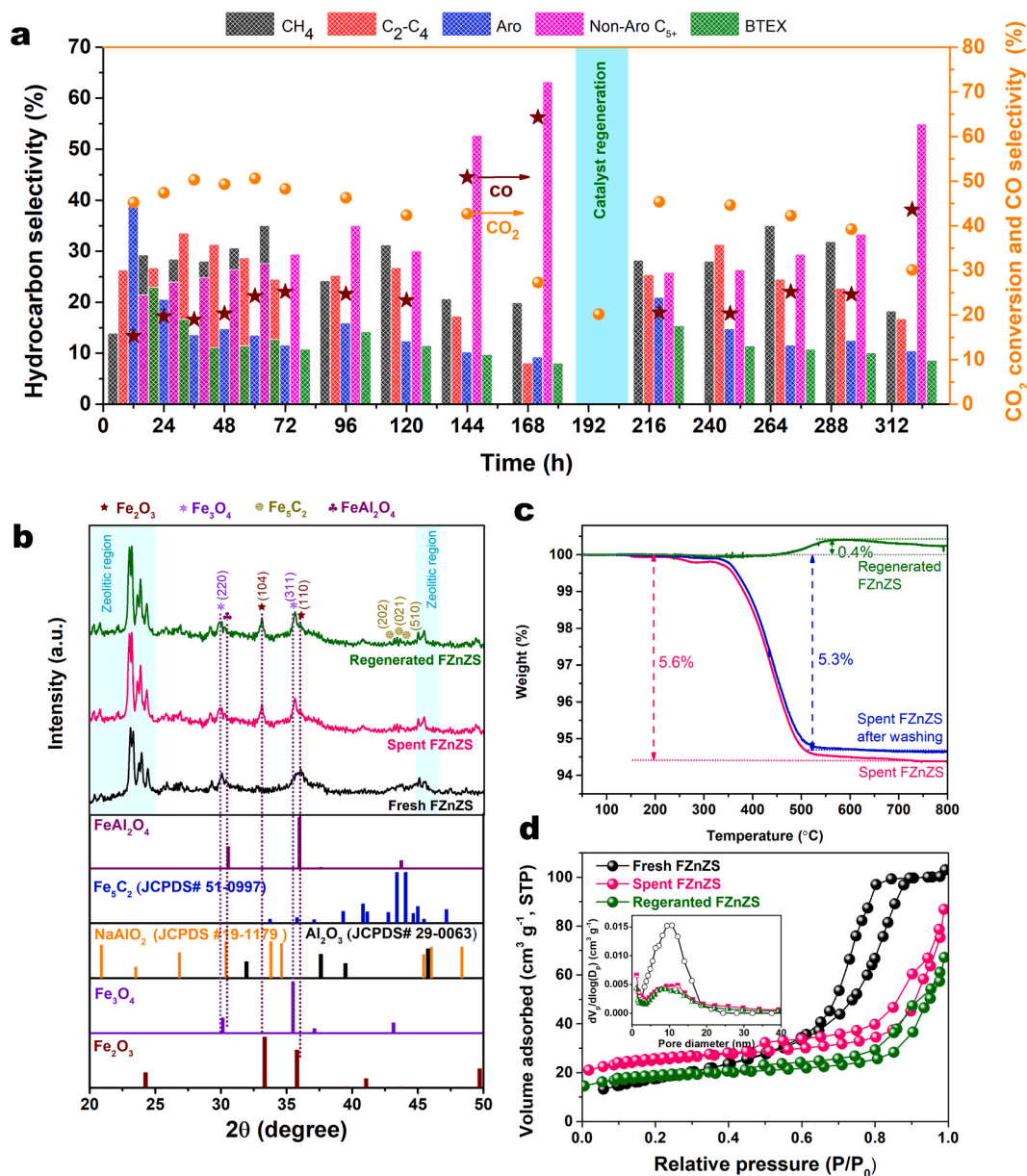


Fig. 8. (a) Long-term stability of the FZnZS catalyst, (b) XRD pattern, (c) TGA profiles, and (d) N₂ adsorption-desorption isotherms and pore size distribution of the fresh, spent, and regenerated FZnZS catalysts.

interparticle agglomeration of the Fe-based particle phase during CO₂ conversion decreased the BET surface area and porosity of the spent catalyst (Fig. 8c). As expected, the BET surface area of the regenerated catalyst was much lower than that of the fresh catalyst due to this interparticle agglomeration (Table S2).

Coke formation during aromatization is known to be responsible for poisoning active sites or blocking micropores (or both) in the zeolite and metal oxides. The BASs of the zeolite are the primary active sites for the generation of coke because of their ability to continue the oligomerization of alkenes and also the dimerization of benzene [98,99]. The thermogravimetric analysis (TGA) profile of the spent catalyst collected after 172 h on stream exhibited a weight loss of 5.6 wt%. After washing with dichloromethane (DCM), the weight loss decreased slightly to 5.3 wt%. Thus, polynuclear aromatics or polymerized species with very low solubilities in DCM were deposited on the spent FZnZS catalyst. In addition, the presence of coke on the surface of Na-FeAlO_x (Fig. S21) could contribute to the total amount of coke on the FZnZS catalyst. HAADF-STEM images of the spent catalyst were acquired to examine

the distribution of elements (Fig. S22). A strong positional correlation between Al and C was observed, indicating the preferential formation of coke on the BASs of the zeolite. In addition, the uneven distribution of Al and Si implies a certain degree of dealumination from the zeolitic structure, resulting in the formation of an extra framework of aluminum ions during CO₂ hydrogenation. This could be attributed to the water that formed as a byproduct of RWGS. However, the change in the crystallinity of the zeolitic structure in the spent and regenerated catalysts was negligible (Fig. 8b), and thus, the overall loss of aluminum ions from the zeolitic structure could also be considered negligible.

4. Conclusions

In summary, we demonstrated the direct conversion of CO₂ to BTEX in high yield over a tandem Na-FeAlO_x/Zn-HZSM-5(12.5)/SiO₂ catalyst in close proximity to the Fe and zeolite sites. Owing to the presence of an amorphous and acidic AlO_x phase, olefin-rich C₂+ hydrocarbons were produced with high selectivity (83.2%) over the Na-FeAlO_x

catalyst at a CO₂ conversion of 47.9% at 370 °C and 3.5 MPa. After achieving close contact between Na-FeAlO_x and Zn-HZSM-5(12.5)@SiO₂ by mortar mixing, the olefin-rich C₂₊ hydrocarbons were converted into high-yield BTEX with an STY of 4.0 mmol g⁻¹ h⁻¹ at a CO₂ conversion of 45.2%. Zn-doping suppressed the BASs in the micropores of HZSM-5, whereas the SiO₂ coating suppressed the BASs on its external surface, thereby enhancing the BTEX selectivity. In situ operando DRIFTS analysis revealed that Zn-HZSM-5(12.5)@SiO₂ played multiple roles in converting CO₂ to aromatics, not only as a site for dehydroaromatization, but also in CO₂ adsorption, in RWGS reactions, and in C-C coupling reactions. Therefore, CO₂ adsorption and the RWGS reaction were significantly activated over the Na-FeAlO_x/Zn-HZSM-5(12.5)@SiO₂ catalyst than over the Na-FeAlO_x catalyst, indicating the synergistic effect between the Na-FeAlO_x and Zn-HZSM-5(12.5)@SiO₂ sites in activating CO₂ hydrogenation. This study not only provides a potential strategy to design a tandem catalyst for the direct conversion of CO₂ to BTEX in high yield, but also provides novel insights into the reaction intermediates on this tandem catalyst. The findings will aid in the development of high-performance catalytic systems to realize a carbon-neutral society.

CRedit authorship contribution statement

Malayil Gopalan Sibi: Conceptualization, Methodology, Formal analysis, Data curation, Writing – original draft. **Muhammad Kashif Khan:** Conceptualization, Methodology, Data curation, Investigation. **Deepak Verma:** Validation, Data curation, Visualization. **Wonjoong Yoon:** Methodology, Formal analysis, Investigation. **Jaehoon Kim:** Supervision, Project administration, Resources, Writing – review & editing Funding acquisition.

Declaration of Competing Interest

The authors declare that they have no known competing financial interests or personal relationships that could have appeared to influence the work reported in this paper.

Acknowledgements

The authors would like to acknowledge financial support received from the National Research Foundation under the “Next Generation Carbon Upcycling Project” (Project No. 2019M1A2A6071810) of the Ministry of Science and ICT, Republic of Korea. Additional support from a National Research Foundation of Korea (NRF) grant funded by the Ministry of Science and ICT, Republic of Korea is also acknowledged (grant number 2020H1D3A1A02079883).

Appendix A. Supporting information

Supplementary data associated with this article can be found in the online version at [doi:10.1016/j.apcatb.2021.120813](https://doi.org/10.1016/j.apcatb.2021.120813).

References

- [1] S. Roy, A. Cherevotan, S.C. Peter, Thermochemical CO₂ hydrogenation to single carbon products: scientific and technological challenges, *ACS Energy Lett.* 3 (2018) 1938–1966.
- [2] A. Modak, P. Bhanja, S. Dutta, B. Chowdhury, A. Bhaumik, Catalytic reduction of CO₂ into fuels and fine chemicals, *Green. Chem.* 22 (2020) 4002–4033.
- [3] M. Aresta, A. Dibenedetto, A. Angelini, Catalysis for the valorization of exhaust carbon: from CO₂ to chemicals, materials, and fuels. Technological use of CO₂, *Chem. Rev.* 114 (2014) 1709–1742.
- [4] P. Gao, S. Li, X. Bu, S. Dang, Z. Liu, H. Wang, L. Zhong, M. Qiu, C. Yang, J. Cai, Direct conversion of CO₂ into liquid fuels with high selectivity over a bifunctional catalyst, *Nat. Chem.* 9 (2017) 1019–1024.
- [5] Z. Li, J. Wang, Y. Qu, H. Liu, C. Tang, S. Miao, Z. Feng, H. An, C. Li, Highly selective conversion of carbon dioxide to lower olefins, *ACS Catal.* 7 (2017) 8544–8548.
- [6] M.K. Khan, P. Butolia, H. Jo, M. Irshad, D. Han, K.-W. Nam, J. Kim, Selective conversion of carbon dioxide into liquid hydrocarbons and long-chain α -olefins over fe-amorphous AlO_x bifunctional catalysts, *ACS Catal.* 10 (2020) 10325–10338.
- [7] Z. He, M. Cui, Q. Qian, J. Zhang, H. Liu, B. Han, Synthesis of liquid fuel via direct hydrogenation of CO₂, *PNAS* 116 (2019) 12654–12659.
- [8] J. Wei, R. Yao, Q. Ge, Z. Wen, X. Ji, C. Fang, J. Zhang, H. Xu, J. Sun, Catalytic hydrogenation of CO₂ to isoparaffins over Fe-based multifunctional catalysts, *ACS Catal.* 8 (2018) 9958–9967.
- [9] L. Wang, S. He, L. Wang, Y. Lei, X. Meng, F.-S. Xiao, Cobalt–nickel catalysts for selective hydrogenation of carbon dioxide into ethanol, *ACS Catal.* 9 (2019) 11335–11340.
- [10] C.-S. Li, G. Melaet, W.T. Ralston, K. An, C. Brooks, Y. Ye, Y.-S. Liu, J. Zhu, J. Guo, S. Alayoglu, High-performance hybrid oxide catalyst of manganese and cobalt for low-pressure methanol synthesis, *Nat. Commun.* 6 (2015) 1–5.
- [11] Y. Ni, Z. Chen, Y. Fu, Y. Liu, W. Zhu, Z. Liu, Selective conversion of CO₂ and H₂ into aromatics, *Nat. Commun.* 9 (2018) 1–7.
- [12] Z. Li, Y. Qu, J. Wang, H. Liu, M. Li, S. Miao, C. Li, Highly selective conversion of carbon dioxide to aromatics over tandem catalysts, *Joule* 3 (2019) 570–583.
- [13] X. Cui, P. Gao, S. Li, C. Yang, Z. Liu, H. Wang, L. Zhong, Y. Sun, Selective production of aromatics directly from carbon dioxide hydrogenation, *ACS Catal.* 9 (2019) 3866–3876.
- [14] J. Wei, R. Yao, Q. Ge, D. Xu, C. Fang, J. Zhang, H. Xu, J. Sun, Precisely regulating Brønsted acid sites to promote the synthesis of light aromatics via CO₂ hydrogenation, *Appl. Catal. B-Environ.* 283 (2010), 119648.
- [15] X. Du, B. Yao, S. Gonzalez-Cortes, V. Kuznetsov, H. AlMegren, T. Xiao, P. Edwards, Catalytic dehydrogenation of propane by carbon dioxide: a medium-temperature thermochemical process for carbon dioxide utilisation, *Faraday Discuss.* 183 (2015) 161–176.
- [16] Y. Wang, W. Gao, S. Kazumi, H. Li, G. Yang, N. Tsubaki, Direct and oriented conversion of CO₂ into value-added, *Aromat., Chem. Eur. J.* 25 (2019) 5149–5153.
- [17] Y. Wang, S. Kazumi, W. Gao, X. Gao, H. Li, X. Guo, Y. Yoneyama, G. Yang, N. Tsubaki, Direct conversion of CO₂ to aromatics with high yield via a modified Fischer-Tropsch synthesis pathway, *Appl. Catal. B-Environ.* 269 (2020), 118792.
- [18] A. Ramirez, A. Dutta Chowdhury, A. Dokania, P. Cnudde, M. Caglayan, I. Yarulina, E. Abou-Hamad, L. Gevers, S. Ould-Chikh, K. De Wispelaere, Effect of zeolite topology and reactor configuration on the direct conversion of CO₂ to light olefins and aromatics, *ACS Catal.* 9 (2019) 6320–6334.
- [19] Y. Xu, T. Wang, C. Shi, B. Liu, F. Jiang, X. Liu, Experimental investigation on the two-sided effect of acidic HZSM-5 on the catalytic performance of composite Fe-based fischer-tropsch catalysts and HZSM-5 zeolite in the production of aromatics from CO₂/H₂, *Ind. Eng. Chem. Res.* 59 (2020) 8581–8591.
- [20] S. Wang, T. Wu, J. Lin, J. Tian, Y. Ji, Y. Pei, S. Yan, M. Qiao, H. Xu, B. Zong, FeK on 3D graphene-zeolite tandem catalyst with high efficiency and versatility in direct CO₂ conversion to aromatics, *ACS Sustain. Chem. Eng.* 7 (2019) 17825–17833.
- [21] C. Zhou, J. Shi, W. Zhou, K. Cheng, Q. Zhang, J. Kang, Y. Wang, Highly active ZnO-ZrO₂ aerogels integrated with H-ZSM-5 for aromatics synthesis from carbon dioxide, *ACS Catal.* 10 (2019) 302–310.
- [22] J. Zhang, M. Zhang, S. Chen, X. Wang, Z. Zhou, Y. Wu, T. Zhang, G. Yang, Y. Han, Y. Tan, Hydrogenation of CO₂ into aromatics over a ZnCrO_x-zeolite composite catalyst, *Chem. Commun.* 55 (2019) 973–976.
- [23] Y. Wang, L. Tan, M. Tan, P. Zhang, Y. Fang, Y. Yoneyama, G. Yang, N. Tsubaki, Rationally designing bifunctional catalysts as an efficient strategy to boost CO₂ hydrogenation producing value-added aromatics, *ACS Catal.* 9 (2018) 895–901.
- [24] Y. Xu, C. Shi, B. Liu, T. Wang, J. Zheng, W. Li, D. Liu, X. Liu, Selective production of aromatics from CO₂, *Catal. Sci. Technol.* 9 (2019) 593–610.
- [25] X. Zhang, A. Zhang, X. Jiang, J. Zhu, J. Liu, J. Li, G. Zhang, C. Song, X. Guo, Utilization of CO₂ for aromatics production over ZnO/ZrO₂-ZSM-5 tandem catalyst, *J. CO₂ Util.* 29 (2019) 140–145.
- [26] J. Wei, Q. Ge, R. Yao, Z. Wen, C. Fang, L. Guo, H. Xu, J. Sun, Directly converting CO₂ into a gasoline fuel, *Nat. Commun.* 8 (2017) 1–9.
- [27] Y. Zhou, H. Thirumalai, S.K. Smith, K.H. Whitmire, J. Liu, A.I. Frenkel, L. C. Grabow, J.D. Rimer, Ethylene dehydroaromatization over Ga-ZSM-5 catalysts: nature and role of gallium speciation, *Angew. Chem. Int. Ed.* 59 (2020) 19592–19601.
- [28] S. Zheng, H.R. Heydenrych, A. Jentys, J.A. Lercher, Influence of surface modification on the acid site distribution of HZSM-5, *J. Phys. Chem. B* 106 (2002) 9552–9558.
- [29] H. Fan, X. Nie, H. Wang, M.J. Janik, C. Song, X. Guo, Mechanistic understanding of ethane dehydrogenation and aromatization over Zn/ZSM-5: effects of Zn modification and CO₂ co-reactant, *Catal. Sci. Technol.* 10 (2020) 8359–8373.
- [30] J.A. Biscardi, G.D. Meitzner, E. Iglesia, Structure and density of active Zn species in Zn/H-ZSM5 propane aromatization catalysts, *J. Catal.* 179 (1998) 192–202.
- [31] S.M. Almutairi, B. Mezari, P.C. Magusin, E.A. Pidko, E.J. Hensen, Structure and reactivity of Zn-modified ZSM-5 zeolites: the importance of clustered cationic Zn complexes, *ACS Catal.* 2 (2012) 71–83.
- [32] Z.N. Lashchinskaya, A.A. Gabrienko, S.S. Arzumano, A.A. Kolganov, A. V. Toktarev, D. Freude, J. Haase, A.G. Stepanov, Which species, Zn²⁺ cations or ZnO clusters, are more efficient for olefin aromatization? ¹³C solid-state NMR investigation of n-But-1-ene transformation on Zn-modified zeolite, *ACS Catal.* 10 (2020) 14224–14233.
- [33] M.G. Ruiz, D.A.S. Casados, J.A. Pliego, C.M. Álvarez, E.S. de Andrés, D.S. Tartalo, R.S. Vague, M.G. Casas, ZSM-5 zeolites modified with Zn and their effect on the crystal size in the conversion of methanol to light aromatics (MTA), *React. Kinet. Mech. Catal.* 129 (2020) 471–490.
- [34] D. Freeman, R.P. Wells, G.J. Hutchings, Conversion of methanol to hydrocarbons over Ga₂O₃/H-ZSM-5 and Ga₂O₃/WO₃ catalysts, *J. Catal.* 205 (2002) 358–365.

- [35] A. Samanta, X. Bai, B. Robinson, H. Chen, J. Hu, Conversion of light alkane to value-added chemicals over ZSM-5/metal promoted catalysts, *Ind. Eng. Chem. Res.* 56 (2017) 11006–11012.
- [36] L. Vosmerikova, Y.E. Barbashin, A. Vosmerikov, Catalytic aromatization of ethane on zinc-modified zeolites of various framework types, *Pet. Chem.* 54 (2014) 420–425.
- [37] V.R. Choudhary, A.K. Kinage, T.V. Choudhary, Effective low-temperature aromatization of ethane over H-gallosilicic acid (MFI) zeolites in the presence of higher alkanes or olefins, *Angew. Chem. Int. Ed.* 36 (1997) 1305–1308.
- [38] A. Mehdad, N.S. Gould, B. Xu, R.F. Lobo, Effect of steam and CO₂ on ethane activation over Zn-ZSM-5, *Catal. Sci. Technol.* 8 (2018) 358–366.
- [39] J. Liu, N. He, Z. Zhang, J. Yang, X. Jiang, Z. Zhang, J. Su, M. Shu, R. Si, G. Xiong, Highly-dispersed zinc species on zeolites for the continuous and selective dehydrogenation of ethane with CO₂ as a soft oxidant, *ACS Catal.* 11 (2021) 2819–2830.
- [40] T. Liang, S. Fadaeayerani, J. Shan, T. Li, H. Wang, J. Cheng, H. Toghiani, Y. Xiang, Ethane aromatization over Zn-HZSM-5: early-stage acidity/performance relationships and deactivation kinetics, *Ind. Eng. Chem. Res.* 58 (2019) 17699–17708.
- [41] J. Liu, N. He, W. Zhou, L. Lin, G. Liu, C. Liu, J. Wang, Q. Xin, G. Xiong, H. Guo, Isobutane aromatization over a complete Lewis acid Zn/HZSM-5 zeolite catalyst: performance and mechanism, *Catal. Sci. Technol.* 8 (2018) 4018–4029.
- [42] S. Tamiyakul, T. Sooknoi, L.L. Lobban, S. Jongpatiwut, Generation of reductive Zn species over Zn/HZSM-5 catalysts for n-pentane aromatization, *Appl. Catal. A Gen.* 525 (2016) 190–196.
- [43] F. Solymosi, A. Széchenyi, Aromatization of n-butane and 1-butene over supported Mo₂C catalyst, *J. Catal.* 223 (2004) 221–231.
- [44] E.A. Pidko, R.A. Van Santen, Activation of light alkanes over zinc species stabilized in ZSM-5 zeolite: a comprehensive DFT study, *J. Phys. Chem. C* 111 (2007) 2643–2655.
- [45] J.A. Biscardi, E. Iglesia, Reaction pathways and rate-determining steps in reactions of alkanes on H-ZSM5 and Zn/H-ZSM5 catalysts, *J. Catal.* 182 (1999) 117–128.
- [46] A.G. Stepanov, S.S. Arzumanov, A.A. Gabrienko, V.N. Parmon, I.I. Ivanova, D. Freude, Significant influence of Zn on activation of the CH bonds of small alkanes by Brønsted acid sites of zeolite, *Acta Phys.-Chim. Sin.* 9 (2008) 2559–2563.
- [47] J.A. Biscardi, E. Iglesia, Structure and function of metal cations in light alkane reactions catalyzed by modified H-ZSM5, *Catal. Today* 31 (1996) 207–231.
- [48] Y. Ono, Transformation of lower alkanes into aromatic hydrocarbons over ZSM-5 zeolites, *Catal. Rev.* 34 (1992) 179–226.
- [49] C.D. Baertsch, H.H. Funke, J.L. Falconer, R.D. Noble, Permeation of aromatic hydrocarbon vapors through silicalite-zeolite membranes, *J. Phys. Chem.* 100 (1996) 7676–7679.
- [50] J. Zhang, W. Qian, C. Kong, F. Wei, Increasing para-xylene selectivity in making aromatics from methanol with a surface-modified Zn/P/ZSM-5 catalyst, *ACS Catal.* 5 (2015) 2982–2988.
- [51] Y. Takamitsu, K. Yamamoto, S. Yoshida, H. Ogawa, T. Sano, Effect of crystal size and surface modification of ZSM-5 zeolites on conversion of ethanol to propylene, *J. Porous Mater.* 21 (2014) 433–440.
- [52] N. Chen, N. Wang, Y. Ren, H. Tominaga, E.W. Qian, Effect of surface modification with silica on the structure and activity of Pt/ZSM-22@SiO₂ catalysts in hydrodeoxygenation of methyl palmitate, *J. Catal.* 345 (2017) 124–134.
- [53] T. Masuda, Diffusion mechanisms of zeolite catalysts, *Catal. Surv. Asia* 7 (2003) 133–144.
- [54] S.J. Han, S.-M. Hwang, H.-G. Park, C. Zhang, K.-W. Jun, S.K. Kim, Identification of active sites for CO₂ hydrogenation in Fe catalysts by first-principles microkinetic modelling, *J. Mater. Chem. A* 8 (2020) 13014–13023.
- [55] C. Yang, H. Zhao, Y. Hou, D. Ma, Fe₃C₂ nanoparticles: a facile bromide-induced synthesis and as an active phase for Fischer–Tropsch synthesis, *J. Am. Chem. Soc.* 134 (2012) 15814–15821.
- [56] J. Liu, G. Zhang, X. Jiang, J. Wang, C. Song, X. Guo, Insight into the role of Fe₃C₂ in CO₂ catalytic hydrogenation to hydrocarbons, *Catal. Today* 371 (2020) 162–170.
- [57] A. Ramirez, L. Gevers, A. Bavykina, S. Ould-Chikh, J. Gascon, Metal organic framework-derived iron catalysts for the direct hydrogenation of CO₂ to short chain olefins, *ACS Catal.* 8 (2018) 9174–9182.
- [58] M. Fleisher, V. Stonkus, L. Leite, E. Lukevics, Investigation of the 1, 4-butanediol dehydrogenation over SiO₂ using AMI method, *Int. J. Quantum Chem.* 100 (2004) 407–411.
- [59] E.A. Wovchko, J.C. Camp, J.A. Glass Jr, J.T. Yates, Active sites on SiO₂: role in CH₃OH decomposition, *Langmuir* 11 (1995) 2592–2599.
- [60] K. Hadjiivanov, Identification and characterization of surface hydroxyl groups by infrared spectroscopy, *Adv. Catal.* 57 (2014) 99–318.
- [61] F. Yi, Y. Chen, Z. Tao, C. Hu, X. Yi, A. Zheng, X. Wen, Y. Yun, Y. Yang, Y. Li, Origin of weak Lewis acids on silanol nests in dealuminated zeolite Beta, *J. Catal.* 385 (2020) 345–346.
- [62] H. Berndt, G. Lietz, J. Völter, Zinc promoted H-ZSM-5 catalysts for conversion of propane to aromatics II. Nature of the active sites and their activation, *Appl. Catal. A-Gen.* 146 (1996) 365–379.
- [63] B. Morrow, I. Cody, Infrared studies of reactions on oxide surfaces. 5 Lewis acid sites on dehydroxylated silica, *J. Phys. Chem.* 80 (1976) 1995–1998.
- [64] N. Lohitham, J.G. Goodwin Jr, Impact of Cr, Mn and Zr addition on Fe Fischer–Tropsch synthesis catalysts: Investigation at the active site level using SSITKA, *J. Catal.* 257 (2008) 142–151.
- [65] W. Wu, E. Weitz, Modification of acid sites in ZSM-5 by ion-exchange: an in-situ FTIR study, *Appl. Surf. Sci.* 316 (2014) 405–415.
- [66] M.I. Zaki, M.A. Hasan, F.A. Al-Sagheer, L. Pasupulety, In situ FTIR spectra of pyridine adsorbed on SiO₂–Al₂O₃, TiO₂, ZrO₂ and CeO₂: general considerations for the identification of acid sites on surfaces of finely divided metal oxides, *Colloids Surf. A Physicochem. Eng. Asp.* 190 (2001) 261–274.
- [67] K. Coenen, F. Gallucci, B. Mezari, E. Hensen, M. van Sint Annaland, An in-situ IR study on the adsorption of CO₂ and H₂O on hydrotalcites, *J. CO₂ Util.* 24 (2018) 228–239.
- [68] E.M. Wilcox, G.W. Roberts, J.J. Spivey, Direct catalytic formation of acetic acid from CO₂ and methane, *Catal. Today* 88 (2003) 83–90.
- [69] C. Johnston, N. Jorgensen, C.H. Rochester, Infrared study of ammonia–carbon monoxide reactions on silica-supported iron catalysts, *J. Chem. Soc., Faraday Trans. 84* (1988) 3605–3613.
- [70] A. Wielers, A. Kock, C. Hop, J. Geus, A. van Der Kraan, The reduction behavior of silica-supported and alumina-supported iron catalysts: A Mössbauer and infrared spectroscopic study, *J. Catal.* 117 (1989) 1–18.
- [71] J.B. Benziger, L.R. Larson, An infrared spectroscopy study of the adsorption of CO on Fe/MgO, *J. Catal.* 77 (1982) 550–553.
- [72] F. Cheng, Q. Cao, Y. Guan, H. Cheng, X. Wang, J.D. Miller, FTIR analysis of water structure and its influence on the flotation of arcanite (K₂SO₄) and epsomite (MgSO₄·7H₂O), *Int. J. Miner. Process.* 122 (2013) 36–42.
- [73] A. Hakim, T.S. Marliza, N.M. Abu Tahari, R.W. Wan Isahak, R.M. Yusop, W. M. Mohamed Hisham, A.M. Yarmo, Studies on CO₂ adsorption and desorption properties from various types of iron oxides (FeO, Fe₂O₃, and Fe₃O₄), *Ind. Eng. Chem. Res.* 55 (2016) 7888–7897.
- [74] J. Baltrusaitis, J. Schuttlefield, E. Zeitler, V.H. Grassian, Carbon dioxide adsorption on oxide nanoparticle surfaces, *Chem. Eng. J.* 170 (2011) 471–481.
- [75] G. Busca, V. Lorenzelli, Infrared spectroscopic identification of species arising from reactive adsorption of carbon oxides on metal oxide surfaces, *Mater. Chem.* 7 (1982) 89–126.
- [76] J. Coates, Interpretation of infrared spectra, a practical approach, *Encycl. Anal. Chem.: Appl., Theory Instrum.* 1 (2006).
- [77] J. Szanyi, J.H. Kwak, Dissecting the steps of CO₂ reduction: 1. The interaction of CO and CO₂ with γ-Al₂O₃: an in situ FTIR study, *Phys. Chem. Chem. Phys.* 16 (2014) 15117–15125.
- [78] X. Wang, M. Shen, L. Song, Y. Su, J. Wang, Surface basicity on bulk modified phosphorus alumina through different synthesis methods, *Phys. Chem. Chem. Phys.* 13 (2011) 15589–15596.
- [79] A.M. Turek, I.E. Wachs, E. DeCanio, Acidic properties of alumina-supported metal oxide catalysts: an infrared spectroscopy study, *J. Phys. Chem.* 96 (1992) 5000–5007.
- [80] G. Lebron, T. Tan, Integrated band intensities of ethylene (12C₂H₄) by Fourier transform infrared spectroscopy, *Int. J. Spectrosc.* (2012) 0 (2012).
- [81] J. Baltrusaitis, J.H. Jensen, V.H. Grassian, FTIR spectroscopy combined with isotope labeling and quantum chemical calculations to investigate adsorbed bicarbonate formation following reaction of carbon dioxide with surface hydroxyl groups on Fe₂O₃ and Al₂O₃, *J. Phys. Chem. B* 110 (2006) 12005–12016.
- [82] H. Knozinger, Acidic and basic properties of aluminas in relation to their properties as catalysts and supports, *Stud. Surf. Sci. Catal.* (1985) 111–125.
- [83] A. Gankanda, D.M. Cwierny, V.H. Grassian, Role of atmospheric CO₂ and H₂O adsorption on ZnO and CuO nanoparticle aging: formation of new surface phases and the impact on nanoparticle dissolution, *J. Phys. Chem. C* 120 (2016) 19195–19203.
- [84] H. Noei, C. Wöll, M. Muhler, Y. Wang, Activation of carbon dioxide on ZnO nanoparticles studied by vibrational spectroscopy, *J. Phys. Chem. C* 115 (2011) 908–914.
- [85] R. Yang, Y. Fu, Y. Zhang, N. Tsubaki, In situ DRIFT study of low-temperature methanol synthesis mechanism on Cu/ZnO catalysts from CO₂-containing syngas using ethanol promoter, *J. Catal.* 228 (2004) 23–35.
- [86] T. Shido, Y. Iwasawa, Reactant-promoted reaction mechanism for water-gas shift reaction on ZnO, as the genesis of surface catalysis, *J. Catal.* 129 (1991) 343–355.
- [87] C. Angell, M. Howell, Infrared spectroscopic investigations of zeolites and adsorbed molecules. Part V. Carbon dioxide, *Can. J. Chem.* 47 (1969) 3831–3836.
- [88] S.-W. Park, O.-S. Joo, K.-D. Jung, H. Kim, S.-H. Han, Development of ZnO/Al₂O₃ catalyst for reverse-water-gas-shift reaction of CAMERE (carbon dioxide hydrogenation to form methanol via a reverse-water-gas-shift reaction) process, *Appl. Catal. A-Gen.* 211 (2001) 81–90.
- [89] J. Pironon, R. Thiery, M. Ayt Ougougal, S. Teinturier, G. Beaudoin, F. Walgenitz, FT-IR measurements of petroleum fluid inclusions: methane, n-alkanes and carbon dioxide quantitative analysis, *Geofluids* 1 (2001) 2–10.
- [90] X. Nie, H. Wang, M.J. Janik, Y. Chen, X. Guo, C. Song, Mechanistic insight into C–C coupling over Fe–Cu bimetallic catalysts in CO₂ hydrogenation, *J. Phys. Chem. C* 121 (2017) 13164–13174.
- [91] G.Q. Zhang, T. Bai, T.F. Chen, W.T. Fan, X. Zhang, Conversion of methanol to light aromatics on Zn-modified nano-HZSM-5 zeolite catalysts, *Ind. Eng. Chem. Res.* 53 (2014) 14932–14940.
- [92] A. Maximov, M. Magomedova, E. Galanova, M. Afokin, D. Ionin, Primary and secondary reactions in the synthesis of hydrocarbons from dimethyl ether over a Pd-Zn-HZSM-5/Al₂O₃ catalyst, *Fuel Process. Technol.* 199 (2020), 106281.
- [93] E. García-Hurtado, A. Rodríguez-Fernández, M. Moliner, C. Martínez, CO₂ hydrogenation using bifunctional catalysts based on K-promoted iron oxide and zeolite: influence of the zeolite structure and crystal size, *Catal. Sci. Technol.* 10 (2020) 5648–5658.
- [94] S. Ilias, A. Bhan, Tuning the selectivity of methanol-to-hydrocarbons conversion on H-ZSM-5 by co-processing olefin or aromatic compounds, *J. Catal.* 290 (2012) 186–192.

- [95] T.E. Tshabalala, M.S. Scurrell, Aromatization of n-hexane over Ga, Mo and Zn modified H-ZSM-5 zeolite catalysts, *Catal. Commun.* 72 (2015) 49–52.
- [96] A. Thivasasith, T. Maihom, S. Pengpanich, J. Limtrakul, C. Wattanakit, Insights into the reaction mechanism of n-hexane dehydroaromatization to benzene over gallium embedded HZSM-5: effect of H₂ incorporated on active sites, *Phys. Chem. Chem. Phys.* 21 (2019) 5359–5367.
- [97] M. Ellouh, Z.S. Qureshi, A. Aitani, M.N. Akhtar, Y. Jin, O. Koseoglu, H. Alasiri, Light paraffinic naphtha to BTX aromatics over metal-modified Pt/ZSM-5, *Chem. Sel.* 5 (2020) 13807–13813.
- [98] M. Guisnet, P. Magnoux, Organic chemistry of coke formation, *Appl. Catal. A-Gen.* 212 (2001) 83–96.
- [99] G. Elordi, M. Olazar, G. Lopez, P. Castaño, J. Bilbao, Role of pore structure in the deactivation of zeolites (HZSM-5, H β and HY) by coke in the pyrolysis of polyethylene in a conical spouted bed reactor, *Appl. Catal. B-Environ.* 102 (2011) 224–231.